Three Dimensional Interferometric Imaging at Terahertz Frequency for Concealed Object Detection

Alexander M. Goltsman
Falls Church, Virginia
November 11, 2011

Thesis submitted to the
faculty of the Virginia Polytechnic Institute and State
University in partial fulfillment of the requirements for
the degree of Master of Science in Electrical Engineering

Amir I. Zaghloul

Tim Pratt

Lamine M. Mili

Keywords: three dimensional imaging, interferometric, interferometry, Terahertz

Abstract

Alexander M. Goltsman

This project was born out of the work performed by a group of researchers at the New Jersey Institute of Technology (NJIT) [1] [2] [3] working on interferometric imaging with a spiral array. Their investigation stopped at two dimensional imaging with a two dimensional array. In this thesis, their idea was developed further into the significantly more complex imaging with a three dimensional array. The general design of the NJIT [1] [2] [3] experiment was reproduced, studied, and modified in a manner that was theorized to enhance the experiment with the added ability to perform three dimensional imaging. The NJIT team [1] [2] [3] has developed their experiment to where they were able to accurately perform two dimensional imaging of two sources of equal intensity located at different distances from a spiral array. In this thesis, the equations used for two dimensional imaging are extrapolated into a three dimensional array application. This three dimensional imaging concept is simulated with MATLAB and the results presented and compared to the NJIT experimental results. [1] [2] [3] A proof of concept physical experiment is conducted and the results are compared to the MATLAB simulation. The results show that additional spatial information can be obtained from a three dimensional array that can enhance the information gleaned from images.

Acknowledgement

I would like to thank and acknowledge the assistance and support of several people that guided me during my work on this thesis.

Dr. Amir I. Zaghloul, my professor and advisor for helping me find the research topic and his considerable help in analyzing and guiding the research.

Dr. Charles Dietlein from Army Research Labs, for his guidance and physical experiment setup and execution.

Dr. David Wikner from Army Research Labs, for his help and support of this project and the experiment.

Dr. Tim Pratt and Dr. Lamine Mili for sitting on my thesis committee.

Dr. John Federici and the NJIT team for providing the inspiration for this thesis.

Cygnus-Quasar Books for providing the rights to reference John D. Kraus's "Radio Astronomy" textbook.

Table of Contents

List of Figures

Chapter 1: Introduction

The goal for this thesis was to investigate and confirm that a three dimensional array used for interferometric imaging performed at terahertz frequency will provide more spatial information about the orientation, location shape and distance to the sources being imaged. The inspiration for the starting point was an experiment performed by a team of researchers at NJIT [1] [2] [3] where they concluded with some testing with a two dimensional spiral array.

The bulk of this thesis is simulation work in MATLAB to recreate the experiments and then increase the scope to three dimensional versions. A proof of concept physical experiment is performed and discussed at the end. To be able to expand on the original two dimensional experiment, it was necessary to recreate it and make sure that the developed simulation was correct and accurately represented the work performed at NJIT. [1] [2] [3]

As a first step, the equations from the two dimensional experiment were used to simulate a one dimensional array imaging one and two sources at different locations. When the simulation results were shown to favorably correlate to the results of the original experiment, the more complex case of a two dimensional array was simulated. Since a spiral array was used in the original experiment, two spiral types, an Archimedean and a Log Periodic, were evaluated for the two dimensional spiral array in the XY plane. The two dimensional array simulation was used to generate images of two sources of equal intensity located at different location in the X, Y and Z domains. The main goal was to investigate how well a two

dimensional array is able to detect changes in perceived intensity between sources that are located at different distances from the imaging array. This simulation is performed with 32 detectors measuring the magnitude and phase of the incident terahertz radiation.

When the two dimensional array simulation was found to correlate favorably with the final results of the original experiment, it was then appropriate to modify and develop the imaging equations further to accommodate a three dimensional array and the more complex computation involved. Beyond the equations, a geometry needed to be developed for the third dimension of the spiral array. Two types of projections of the array in the Z domain were evaluated along with the two types of spiral projections in the X and Y domains. The Archimedean spiral and Log Periodic spirals were once again evaluated in conjunction with linear and log periodic distributions in the negative Z direction. The three dimensional array images were generated and compared with the results of the two dimensional array.

As a final step, a proof of concept physical experiment is performed to compare the simulation results to real world experiment al results. Primarily due to financial constraints, some variables were changed for the physical experiment to accommodate readily available equipment. Another simulation was performed where the simulation variables were adjusted to better represent the proof of concept experiment.

After a brief discussion about Interferometry and Terahertz frequency, this thesis delves into a detailed analysis of each of the simulation and experimental steps discussed. Results are presented and discussed to support the thesis.

Chapter 2: Why Terahertz Frequency?

Terahertz frequency radiation has interested scientists for the past century; however it has not been widely available for study and analysis to science due to high costs of generating and measuring Terahertz frequency radiation. In recent history there has been a dramatic and at times frantic increase in interest in Terahertz frequency study. Terahertz frequency radiation refers to radio waves that come from the region of the electromagnetic spectrum between infrared and microwave radiation.

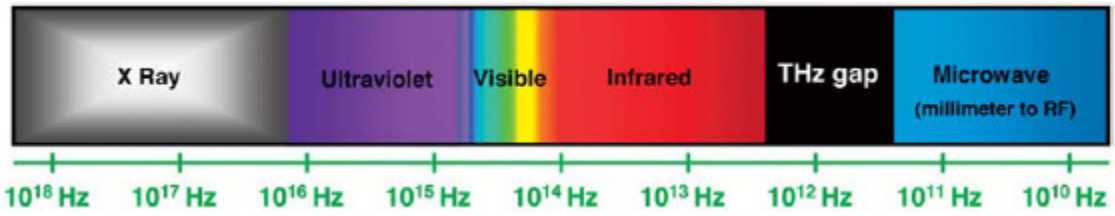

Figure 2.1: Electromagnetic spectrum showing the relative location of the THz band region where much study and interest is centered. [4]

Although it has limitations and challenges for its use, terahertz frequency radiation holds many promises for sensor technology. One of the main drawbacks to terahertz frequency radiation is that due to its high frequency, the attenuation through free space is dramatic. The attenuation becomes even more dramatic through humid air. This causes significant problems for pulsed sensor system where a 1ps pulse enlarges to a 30ps pulse by traveling through just 2.4m of humid atmosphere. [2] This pulse can further enlarge to more than 100ps after 100m of propagation. [2] This is one of the phenomenons that are a challenge to be overcome by pulsed terahertz systems. A continuous wave, or CW terahertz, radiation system does not

use pulsing but rather uses a continuous terahertz radiation wave. Another argument for using CW radiation is that most of the environment around us naturally releases infrared and terahertz radiation. This means that for imaging applications it is not necessary to illuminate the object with radiation and observe the reflection. Usually there is adequate ambient radiation to detect and generate an image.

One of the main advantages of terahertz radiation is that unlike X-rays it is none ionizing. This makes it safe and non-destructive to biological tissue. Where X-rays pass through skin, muscle, and bone, due to their small wavelength of 10 to 0.1 nanometers and ionize tissue due to their high energy; terahertz radiation does not ionize tissue and has a larger wavelength that is sub millimeter range. The terahertz radiation wavelength ranges from one millimeter to 100 micrometers. This is one of the benefits of terahertz radiation in that it can pass through clothing, bags, and luggage, and all things that are non-polar, and it is reflected by polar materials, such as metal, polar chemicals, compounds, and others. Terahertz radiation does not pass through a human being, it is reflected by the skin and surface tissue, and most importantly it does not damage, chemically alter, or harm biological tissue.

Incidentally this is another area for research in terahertz for potential uses, as well as an area for privacy concerns. There have been some expensive imaging systems developed that work based off of different concepts from the ones discussed in this thesis which use higher frequency terahertz radiation in the 300Ghz to 900Ghz range, and use phased arrays and other expensive electromagnetic devices to generate images. These images have caused some concern because as discussed earlier terahertz radiation passes through clothing and is reflected by the skin. This

can generate images of human bodies with enough detail of anatomy to cause concerns about invasion of privacy. Of course not all imaging systems have enough resolution to show such detail, and the resolution can be designed to be low enough to eliminate the potentially embarrassing detail. Since the goal of these imaging systems is security, most detectable objects of concern are relatively large and most importantly would show up much “brighter” on these imaging systems than biological tissue. There has also been some research into using terahertz for imaging and analyzing skin and shallow biological tissue for cancer, damage, and other anomalies.

Chapter 3: Theory of Interferometry

3.1 The Simple (Adding) Interferometer

Increasing the aperture of an antenna has a direct impact on the directivity of the antenna and can typically improve the resolution of the images generated. Large aperture antennas are expensive. Placing two antennas of uniform aperture *a* spaced a distance *s* apart as shown in Figure 3.1 can help recreate images with much better resolution than the aperture *a* antennas individually. Using more than two antennas of aperture *a* and comparing pairs of these antennas can help reproduce the resolution of a large aperture antenna. A pair of antennas of aperture *a* spaced a distance *s* apart creates the autocorrelation function as shown in Figure 3.2. [5]

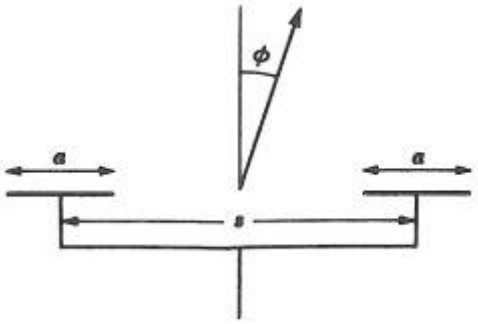

Figure 3.1: Simple Interferometer. Reproduced from reference [5] with permission**.**

By making many observations of these pairs of aperture *a* antennas, or detectors out to s_λ higher spatial-frequency components can be achieved in the observed pattern to a cutoff

$$\chi_{\lambda_c} = s_\lambda + \alpha_\lambda \qquad (3\text{-}1)$$

The angular resolution can be described as

$$\phi_c = \frac{1}{s_\lambda + \alpha_\lambda} rad = \frac{57.3}{s_\lambda + \alpha_\lambda} \deg \tag{3-2}$$

For apertures α_λ that are much smaller than distances s_λ this can be simplified to just s_λ. In interferometry a pair of detectors or antennas separated by a distance s_λ is called a baseline, b

$$\phi_c = \frac{57.3}{b} \deg$$

By making enough observations with enough unique baselines it is possible to reproduce the true brightness distribution of the sources or objects being images. [5]

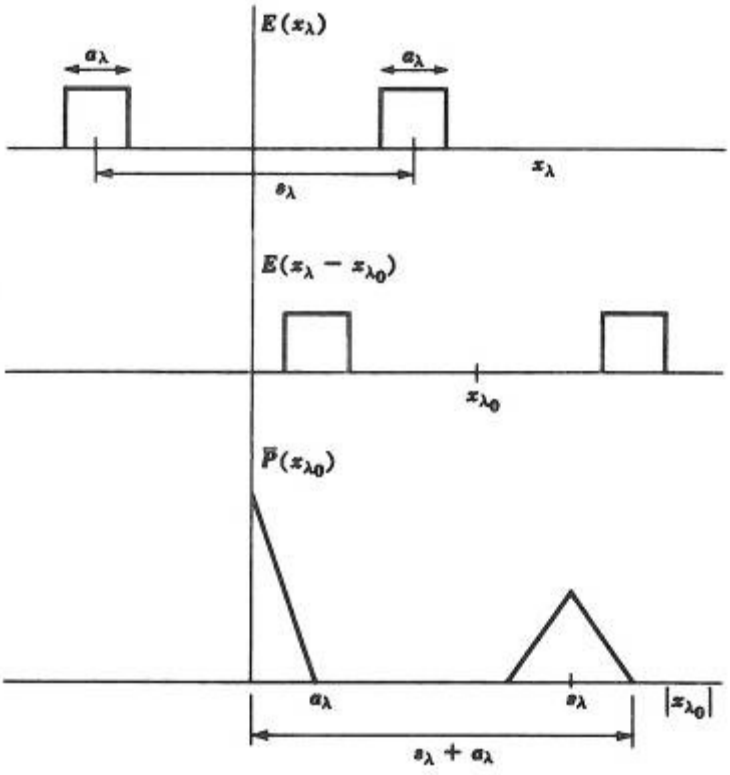

Figure 3.2: Autocorrelation function of aperture distribution of a simple interferometer. Reproduced from reference [5] with permission**.**

Given a normalized far-field pattern of a two-element array given below in 3-3 [5]

$$E(\phi) = E_n(\phi)\cos\left(\frac{\psi}{2}\right) \tag{3-3}$$

where $E_n(\phi)$ is the normalized field patter of an individual array element and $\psi = 2\pi s_\lambda \sin\phi$. The relative power pattern is equal to the square of $|E(\phi)|$, or [5]

$$P(\phi) = \left|E(\phi)\right|^2 = \left|E_n(\phi)\right|^2 \cos^2\frac{\psi}{2} = \frac{\left|E_n(\phi)\right|^2(1+\cos\psi)}{2} \tag{3-4}$$

As in Figure 3.3, the first factor is (3-4) is the element power pattern as graphed in 3.3a, the other factor represents an array of two of these elements as shown in 3.3b. When the element power pattern and the array pattern are multiplied together the result is the pattern shown in 3.3c. Figure 3.3c is the power pattern of the interferometer in Figure 3.1. [5]

$$\begin{aligned} S(\phi_0, s_\lambda) &= \left|E_n(\phi)\right|^2 \int_{-\alpha/2}^{+\partial/2} B(\phi)\{1+\cos[2\pi s_\lambda \sin(\phi_0-\phi)]\}d\phi \\ S(\phi_0, s_{\lambda)} &= \left|E_n(\phi)\right|^2 \left\{S_0 + \int_{-\alpha/2}^{+\alpha/2} B(\phi)\cos[2\pi s_\lambda \sin(\phi_0-\phi)]d\phi\right\} \end{aligned} \tag{3-7}$$

$S(\phi_0,s_\lambda)$ = observed flux density distribution	watts $m^{-2}H^{-1}$
$B(\phi)$ = true source brightness distribution	watts $m^{-2}Hz^{-1}$ sr^{-1}
ϕ_0 = displacement angle	rad
α = source extent	rad
s = interferometer element spacing	
$s_\lambda = s/\lambda$	
S_0 = flux density of source	

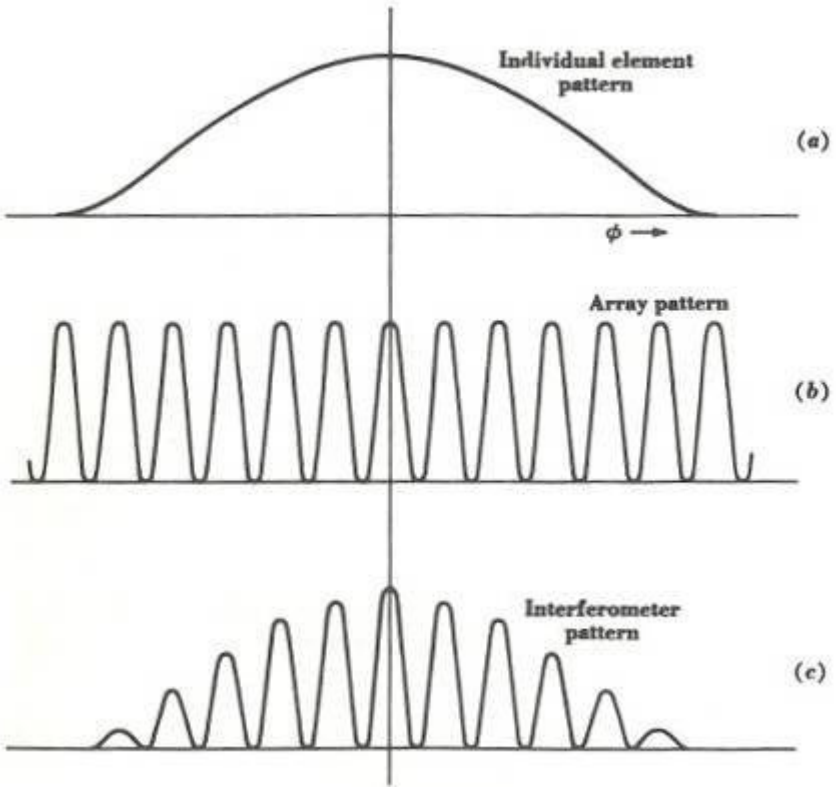

Figure 3.3: (a) Individual element pattern; (b) array pattern; and (c) the resultant interferometer pattern for the case of a point source. Reproduced from reference [5] with permission**.**

Formula 3-7 described the observed flux density distribution which is illustrated for three cases in figure 3.4 below. Figure 3.4a shows the interferometer pattern for the case when the distance to the source is much smaller than the lobe spacing. Figure 3.4b shows the interferometer pattern for the case when the distance to the sources is only slightly smaller than the lobe spacing. Figure 3.4c shows the interferometer pattern for the case when the distance to the sources is equal to the lobe spacing. [5]

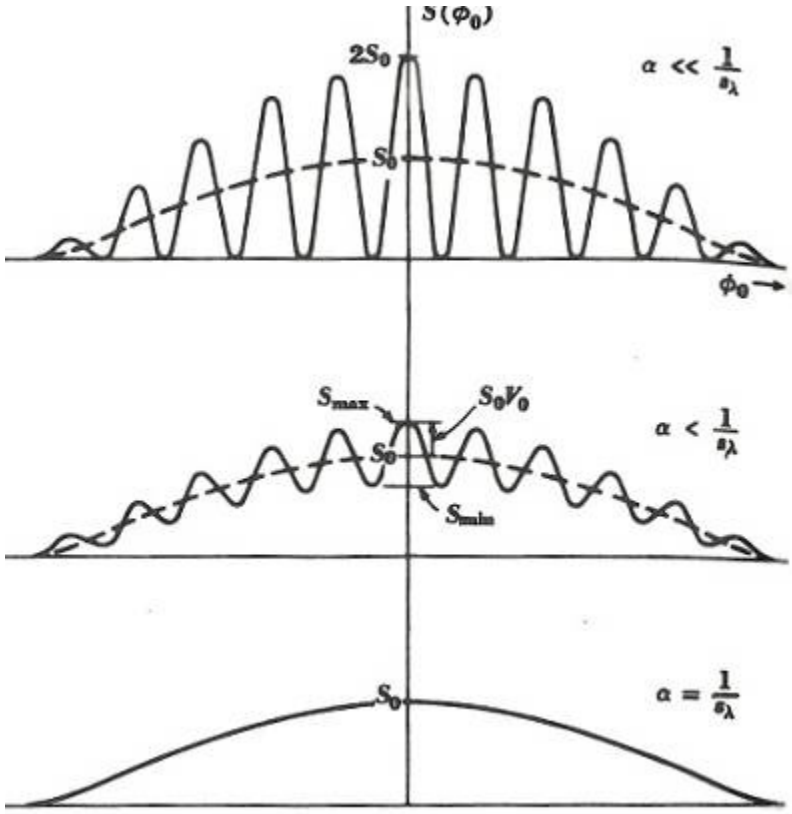

Figure 3.4 Interferometer pattern (a) for point sources; (b) for a uniform extended source of angle $\alpha < 1/s_\lambda$; and (c) for a uniform extended source of angle $\alpha = 1/s_\lambda$. Reproduced from reference [5] with permission**.**

Equation 3-7 can be simplified if the source is assumed to be at the boresight of the interferometer then $|E_n(\phi)|^2 = 1$ and the equation becomes as follows. [5]

$$S(\phi_0, s_\lambda) = S_0 + \int_{-\alpha/2}^{+\alpha/2} B(\phi) \cos\left[2\pi s_\lambda \sin(\phi_0 - \phi)\right] d\phi \qquad (3\text{-}8)$$

If the source is modeled as a point source such that $\phi_0 - \phi << \pi$, we can simplify the equation further. [5]

$$S(\phi_0, s_\lambda) = S_0 + \cos 2\pi s_\lambda \phi_0 \int_{-\alpha/2}^{+\alpha/2} B(\phi) \cos 2\pi s_\lambda \phi d\phi$$

$$+ \sin 2\pi s_\lambda \phi_0 \int_{-\alpha/2}^{+\alpha/2} B(\phi) \sin 2\pi s_\lambda \phi d\phi \qquad (3\text{-}9)$$

The equation 3-9 can be factored to be comprised of a constant term and another equation as in 3-10.

$$S(\phi_0, s_\lambda) = S_0\left[1 + V(\phi_{0,s_\lambda})\right] \tag{3-10}$$

$V(\phi_0,s_\lambda)$ can then be expressed as the equation it replaced.

$$V(\phi_0, s_\lambda) = \frac{1}{S_0}\cos 2\pi s_\lambda \phi_0 \int_{-\alpha/2}^{+\alpha/2} B(\phi)\cos 2\pi s_\lambda \phi d\phi$$

$$+ \frac{1}{S_0}\sin 2\pi s_\lambda \phi_0 \int_{-\alpha/2}^{+\alpha/2} B(\phi)\sin 2\pi s_\lambda \phi d\phi \tag{3-11}$$

This equation can be further developed by changing the sine to a cosine with a phase displacement of $\Delta\phi_0$ as shown below in 3-12 and 3-13. [5]

$$V(\phi_0, s_\lambda) = V_0(s_\lambda)\cos\left[2\pi s_\lambda(\phi_0 - \Delta\phi_0)\right] \tag{3-12}$$

$$V(\phi_0, s_\lambda) = V_0(s_\lambda)(\cos 2\pi s_\lambda \phi_0 \cos 2\pi s_\lambda \Delta\phi_0 + \sin 2\pi s_\lambda \phi_0 \sin 2\pi s_\lambda \Delta\phi_0 \tag{3-13}$$

In equation 3-13 the variable $V_0(s_\lambda)$ corresponds to amplitude of the lobes of the interferometer pattern. $V_0(\phi_0 s_\lambda)$ is also called the *visibility function*. Combining equations 3-11 and 3-13 they can be further developed into 3-16 as shown below in 3-14, 3-15 and 3-16. [5]

$$V_0(s_\lambda)\cos 2\pi s_\lambda \Delta\phi_0 = \frac{1}{S_0}\int_{-\alpha/2}^{+\alpha/2} B(\phi)\cos 2\pi s_\lambda \phi d\phi \tag{3-14}$$

$$V_0(s_\lambda)\sin 2\pi s_\lambda \Delta\phi_0 = \frac{1}{S_0}\int_{-\alpha/2}^{+\alpha/2} B(\phi)\sin 2\pi s_\lambda \phi d\phi \tag{3-15}$$

$$V_0(s_\lambda)e^{j2\pi s_\lambda \Delta\phi_0} = \frac{1}{S_0}\int_{-\alpha/2}^{+\alpha/2} B(\phi)e^{j2\pi s_\lambda \phi} d\phi \tag{3-16}$$

From equation 3-15 where $V_0(\phi_0 s_\lambda)$ is the visibility function can be rewritten as the complex visibility function in 3-16. Assuming a narrow angle to the source the

complex visibility function can be integrated to infinity without introducing any significant error. [5]

$$V_0(s_\lambda)e^{j2\pi s_\lambda \Delta\phi_0} = \frac{1}{S_0}\int_{-\alpha/2}^{+\alpha/2} B(\phi)e^{j2\pi s_\lambda \phi}\,d\phi \qquad (3\text{-}17)$$

From equation 3-17 it is evident that the complex visibility function equals the Fourier transform of the source brightness distribution divided by the flux density of the source, S_0. [5]

$$B(\phi_0) = S_0\int_{-\alpha/2}^{+\alpha/2} V_0(s_\lambda)e^{j2\pi s_\lambda \Delta\phi_0}e^{-j2\pi s_\lambda \phi_0}\,ds_\lambda \qquad (3\text{-}18)$$

$$B(\phi_0) = S_0\int_{-\alpha/2}^{+\alpha/2} V_0(s_\lambda)e^{-j2\pi s_\lambda (\phi_0 - \Delta\phi_0)}\,ds_\lambda \qquad (3\text{-}19)$$

Equation 3-19 above show that the true brightness distribution, $B(\varphi_0)$, of the source can be calculated with a Fourier transform of the complex visibility function. [5]

To improve the accuracy of the obtained true source brightness using a simple interferometer, enough measurements of unique pairs of detectors or baselines need to be made with sufficient unique baseline distances (S_λ). High signal to noise ratio (SNR) and the absence of sources with a high flux density in the individual detector patterns improves the quality of the interferometric image. Because of these factors there are some limitations to the detail of the image that can be obtained from this technique.

Chapter 4: Simulation and Proof of Concept Experiment

The experiment that is used as the starting point in this thesis is the experiment conducted at New Jersey Institute of Technology (NJIT), on the subjects of Terahertz Interferometric imaging, synthetic aperture imaging, and imaging of concealed objects. [1] [2] [3] This experiment has been developed by a group at NJIT since 2004. Their previous papers that are acknowledged and referenced at the end of this thesis dealt with the initial concepts, theories, and derivations, as well as the initial experiments of one dimensional, an two dimensional setups. This experiment continues this investigation with three dimensional array setups, and investigations into log periodic arrangements. [1] [2] [3]

The experimental data was collected on a lab set up similar to the one below in Figure 4.4.

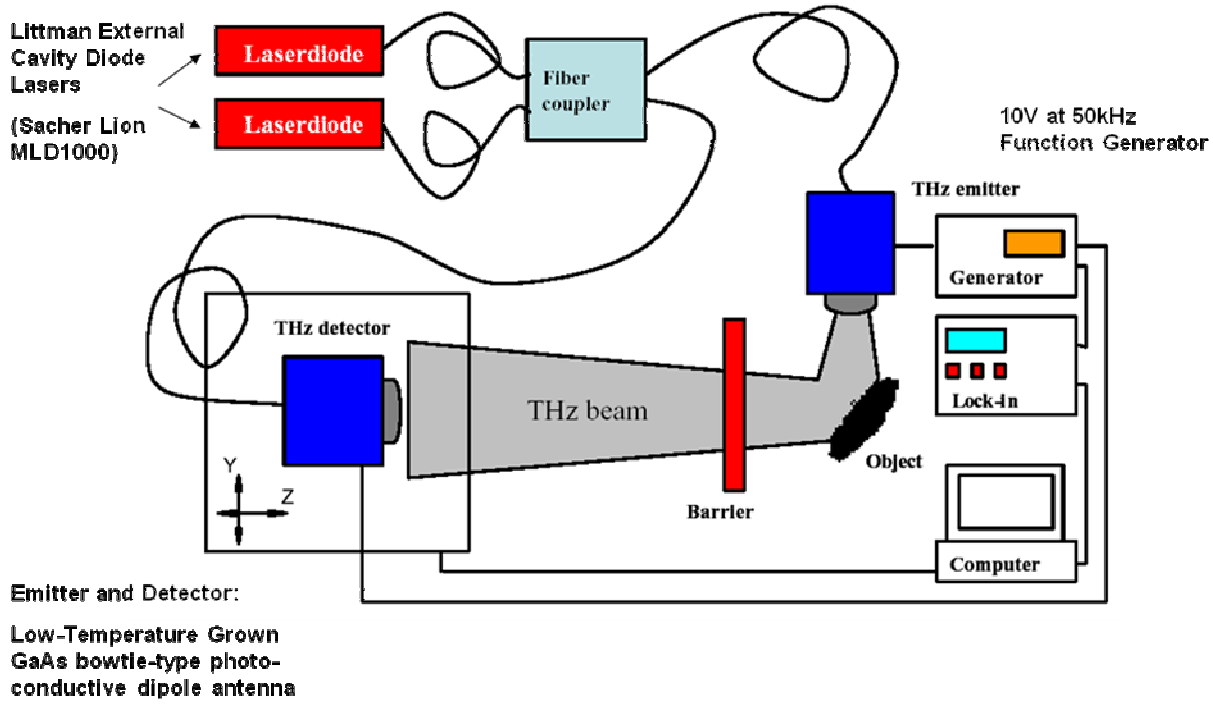

Figure 4.1: The NJIT group's experimental setup. [3]

4.1 Experimental Setup

The experiment used for this thesis is derived from the experiments from [1] [2] [6] and [3]. It consists of 32 detectors located one meter from the source or sources being imaged. Throughout the simulations a frequency of 0.3 THz was used for the sake of standardizing the results for all scenarios and to accurately recreate the results of the experiments from [1] [2] [6] and [3]. In these experiments the array was either linear or a two dimensional spiral in the XY plane. These experiments were recreated and verified the results presented by the experiments from [1] [2] [6] and [3], as well as went beyond the scope of their experiments and derived formulas for a three dimensional array, formulas for imaging with an interferometric three dimensional array, and investigated various configurations of the array in the third dimension such as a log periodic configuration.

These experiments were performed as simulations to reproduce the results from [1] [2] [6] and [3], a simulation of the proposed three dimensional improved array and finally a physical experiment mimicking the three dimensional hypothesis.

The experimental simulations that were conducted can be subdivided into a few categories. Firstly there is the one dimensional case, with all detectors distributed along the X-axis. The second case is two dimensional with two different spiral configurations, one Archimedean spiral and one Log Periodic spiral. In the third case, where the bulk of the work went, the three dimensional case was simulated with both Archimedean and Log Periodic spirals in the XY plane, and three different configurations in the Z-axis. Experimentation was conducted with a linear distribution, as well as a log periodic distribution of the elements in the Z direction.

4.2 Theory

In reproducing the experiment the setup was kept as close as possible to the original experiment to make sure that it would be clear how and why the experiment worked and could reproduce the results. The arrays used are aperiodic and have detector elements spread out in various geometries. The amplitude and phase of the incident terahertz wave at each detector are measured and the values received from all detectors are correlated with each other. Each detector is correlated with all the other detectors once, such that for N detectors there are N(N-1)/2 correlated detector pairs, or baselines. When a Fourier inversion is performed, each of these baselines contribute a Fourier spatial component of the original incident terahertz wave. The correlated Fourier spatial component from each of these baselines corresponds to a point on the U-V plane. This correlated baseline contribution also corresponds to a pixel in the image. Therefore the more baselines, or points on the U-V plane, the better the image quality. [6]

Next issue that must be dealt with is that of the curvature of the incident waves. In the paper referenced at [1], there was extensive description of this issue. In summary, in traditional interferometric applications for radio astronomy the observed incident waves can be assumed to be planar due to the great distances involved between celestial bodies. In security applications the distances between the array and the observed sources are usually closer than 50 meters. In this experiment the arrangement used is for screening individuals at close quarters and thus the distance between the imaging array and the source is about one meter. At such close quarters the incident waves are not in far-field. The incident waves are curved

and must be analyzed in the near-field. In this arrangement it is extremely important to know the exact distance to the source, this however is not a major problem as it is relatively easy to measure the exact distance to the source with modern equipment. The issue with curved incident waves is that if an image was reconstructed from a planar array and near-field curved incident waves it would be distorted due to the aberrations caused by the curvature of the waves.

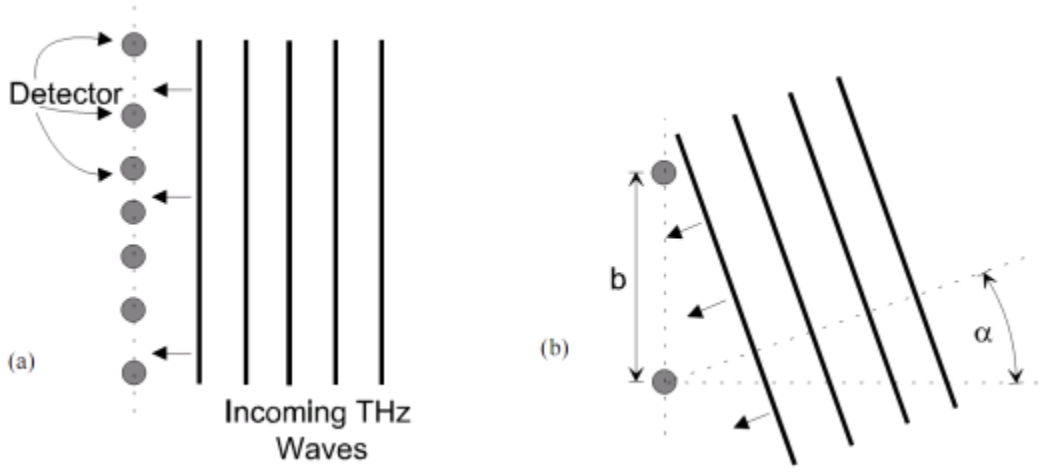

Figure 4.2: This figure shows a planar array with incident planar waves. This is an example of a far field example. [1]

There are two possible solutions to the problem of curved incident waves. One possibility is to deform the shape of the array to be spherical to compensate for the curvature of the incident waves. A simpler and more robust way to compensate is to pre-distort the image by shifting the phase at each detector by a pre-calculated phase correction. [1]

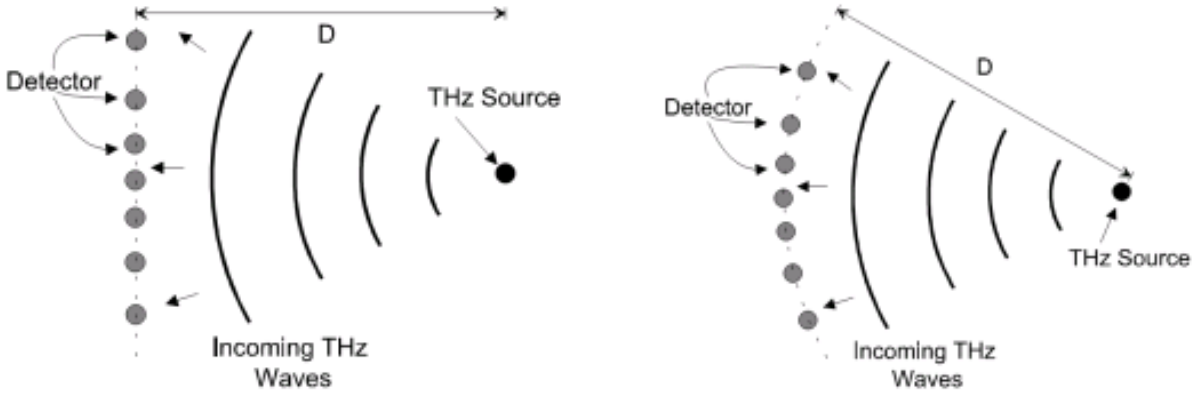

Figure 4.3: This figure depicts curved incident waves on a planar array on the left and a curved array on the right. By applying the calculated phase shift to each detector it is possible to pre-distort a planar array. [1]

The calculation for the phase correction is relatively straight forward and can be performed on the simulation and experimental data. The detectors in the array measure and record the amplitude and phase of the incident waves. It is necessary to pre-distort the received image by applying a calculated phase shift to each detector according to the formula:

$$\phi_{corrected} = \phi_{initial} + k\left(\sqrt{x_l^2 + y_l^2 + z_l^2} + Z_0\right) \qquad (4\text{-}0)$$

The corrected phase angle detected at each detector is calculated from the detected amplitude and phase. This is discussed at great length by the authors of the work referenced at [1]. In the simulation, however, this correction is not implemented for simplifications sake and to isolate and test the qualities and performance of the three dimensional setup proposed by this experiment. It is also deemed not critical to implement this corrective technique as even with a one meter distance between the array and the sources, with an operating frequency of 0.3THz or a wavelength of 0.001 meters, the distance of one meter is about a thousand wavelengths between

the sources and the imaging array. A thousand wavelengths is enough to assume a far field scenario for this simulation. In future calculations if high precision and more analysis is required this correction can be investigated further.

The system simulated in this experiment would in practice use detectors to measure the amplitude and phase of the incident waves to provide the system with data. In this simulation the data that would be provided by these detectors has to be simulated as well. In these experiments the results of imaging systems with both, one and two sources are analyzed and simulated. Once a system that can successfully image more than one source is demonstrated an infinite number of sources or a surface.

In the paper referenced at [3] a derivation is discussed how a system consisting of more than one source can be simulated. These derivations were extended to a three dimensional array system. The detectors that would be used in practice in the simulated system directly measure the amplitude and phase of incident waves. If the system was imaging two or more sources, it would only detect the resultant magnitude and phase of the incident electric field. Therefore in the simulation of this system the resultant electric field of two or more sources would have to be reproduced.

Assuming that two sources, A and B exist they can be described as Green's functions as follows,

$$E_A = \frac{Ae^{ikr}}{r} \qquad \text{and} \qquad (4\text{-}1)$$

$$E_B = \frac{Be^{ik|\bar{r}-\bar{r}_0|}}{|\bar{r}-\bar{r}_0|} \qquad (4\text{-}2)$$

Where A and B are the amplitudes of the two sources, *r* is the distance from the element to source A, and r_0 is the distance from the element to source B. Next are the parameters from [1] [2] [3] and [6] modified for three dimensional array calculations,

$$q_A(n) = r_A = \sqrt{(x(n))^2 + (y(n))^2 + Z_0^{\,2}} \tag{4-3}$$

$$q_B(n) = r_B = \sqrt{(x(n) - x_B)^2 + (y(n) - y_B)^2 + Z_0^{\,2}} \tag{4-4}$$

Where *x(n)* and *y(n)* are the coordinates of the *n*-th detector, x_B and y_B are the x and y coordinates of source B, Z_0 is the distance from the plane of the detector array to the plane of the source, and source A is assumed to be located at $(0,0,Z_0)$. Modifying these parameters for the three dimensional array application yields,

$$q_A(n) = r_A = \sqrt{(x(n) - x_A)^2 + (y(n) - y_A)^2 + (z(n) - z_A)^2} \tag{4-5}$$

$$q_B(n) = r_B = \sqrt{(x(n) - x_B)^2 + (y(n) - y_B)^2 + (z(n) - z_B)^2} \tag{4-6}$$

Where *z(n)* is the z coordinate of the *n*-th detector and x_A, y_A, z_A and x_B, y_B, z_B are the x, y, z coordinates of the sources A and B respectively. Combining the above equations and summing the Green's functions from the two sources A and B, the total electric field incident on the detector array is calculated as follows in [1] [2] [6] and [3],

$$E = E_A + E_B = \frac{Ae^{ikq_A(n)}}{q_A(n)} + \frac{Be^{ikq_B(n)}}{q_B(n)} = Mag\ e^{i\ phase} \tag{4-7}$$

Once the total electric field incident on the detector array has been calculated at each detector the Fourier transform for all baselines is calculated as follows in [1] [2] [6] and [3],

$$\sigma_E(\xi,\eta) = \sum_{l=1}^{N(N-1)/2}\left[\mathrm{Re}\left(A_l e^{i\Delta\phi_l}\right)\cos\left(k\left(u_l\xi + v_l\eta\right)\right) - \mathrm{Im}\left(A_l e^{i\Delta\phi_l}\right)\sin\left(k\left(u_l\xi + v_l\eta\right)\right)\right] \quad (4\text{-}8)$$

Where σ_E is the time-averaged intensity of the source, u_l is $(x_n - x_m)$ and v_l is $(y_n - y_m)$ are the x and y baselines for two detectors located at the points (x_m,y_m) and (x_n,y_n), k is the wave number, N is the number of detectors in the array, A_l is the product of E_mE_n, $\Delta\phi_l$ is $\phi_m - \phi_n$. The variables ξ is x'/Z_0 and η is y'/Z_0 represent the ratio of the source located at (x',y') and Z_0 which is the distance from the detector array to the source plane. [3]

The Fourier transform equation above required some modification to be used in a three dimensional array application. In the modified experiment the constraints on the experiment were made much more flexible. This experiment is designed such that the sources do not have to be in the same plane, they may have different z values, also obviously in three dimensional array the detectors will have different z values as well. In modifying the above equation for three dimensions it was necessary to add another variable w_l which was $(z_n - n_m)$, also Θ was added to represent z'/Z_0 in the equation. Below are the two parts of the above equation, 4-9 and 4-10, that have been modified; they are the Cosine and Sine expressions,

$$\cos\left(k\left(u_l\xi + v_l\eta + w_l\Theta\right)\right) =$$

$$\cos\left(k\left[\left(\frac{x_m x'}{z'-z_m} - \frac{x_n x'}{z'-z_n}\right) + \left(\frac{y_m y'}{z'-z_m} - \frac{y_n y'}{z'-z_n}\right) + \left(\frac{z_m z'}{z'-z_m} - \frac{z_n z'}{z'-z_n}\right)\right]\right) \quad (4\text{-}9)$$

and,

$$\sin\left(k\left(u_l\xi + v_l\eta + w_l\Theta\right)\right) =$$

$$\sin\left(k\left[\left(\frac{x_m x'}{z'-z_m}-\frac{x_n x'}{z'-z_n}\right)+\left(\frac{y_m y'}{z'-z_m}-\frac{y_n y'}{z'-z_n}\right)+\left(\frac{z_m z'}{z'-z_m}-\frac{z_n z'}{z'-z_n}\right)\right]\right) \qquad (4\text{-}10)$$

Substituting in the expanded cosine and sine expressions above into the time-averaged intensity equation mentioned earlier, yields the completed three dimensional expression.

$$\sigma_E(\xi,\eta)=\sum_{l=1}^{N(N-1)/2}\left[\mathrm{Re}\left(A_l e^{i\Delta\phi_l}\right)\cos\left(k\left(u_l\xi+v_l\eta+w_l\Theta\right)\right)-\mathrm{Im}\left(A_l e^{i\Delta\phi_l}\right)\sin\left(k\left(u_l\xi+v_l\eta+w_l\Theta\right)\right)\right] \qquad (4\text{-}11)$$

4.3 One Dimensional Experiment

The first step to adding and expanding to the experiment from [1] [2] [3] and [6] is to recreate it to verify that the proper processes, theories, and formulas were followed. In this experiment that refers to verifying the basic formulas and equations for a one dimensional array, imaging one source located directly above the array at a height of one meter. The distribution of the elements on the one dimensional array was done trying to emulate the one dimensional array used in the original experiment. [6] Figure 4.4 below shows the location of the simulated elements on the X-axis.

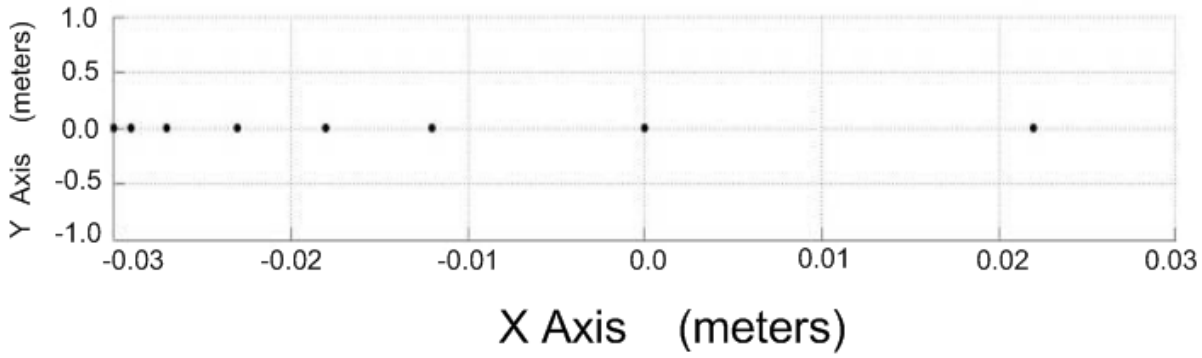

Figure 4.4: One dimensional 8 detector array situated along the X-axis.

4.3.1 Theoretical Explanation

As mentioned above, interferometric image resolution quality is driven primarily by the number of baselines and the differences in length among the baselines. In the one dimensional experiment from [1] [2] [6] and [3], results and procedures were emulated by using a similarly laid out eight element array. An eight

element array pictured above according to the formula N(N-1)/2, yields 28 baselines. As in most of the scenarios discussed in this thesis, the simulations show scenarios for both one and two sources being imaged.

4.3.2 Simulation Results

Initially it is necessary to verify the ability of the array to detect the simplest scenario; this would be detecting one source at the origin 1 meter above the array. For initial simulation and to emulate the results of the one dimensional experimental simulation in [1] [2] [6] and [3], the first image is conducted by setting the $\Delta\phi_l = 0$ of equation (4-8) for simplification as idealization of the scenario. This is shown in Figure 4.5 below.

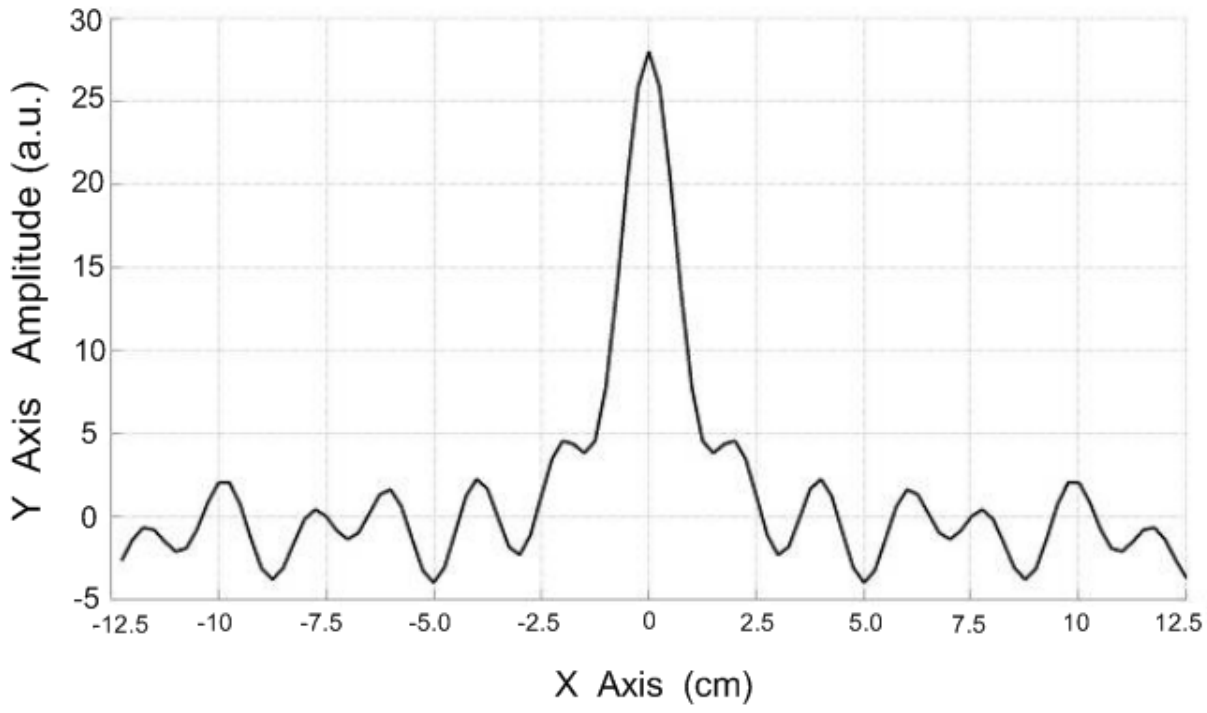

Figure 4.5: One dimensional 8 detector array image of Source A located at (0,0,1) above the array. $\Delta\phi = 0$. The X axis is from 0 to 100 and depicts data points. The data points are spaced 0.0025 meters apart. X axis 0 corresponds to -12.5cm, 50 corresponds to the origin and 100 corresponds to 12.5cm.

When the $\Delta\phi$ is reintroduced into equation (4-8) the image starts to look a bit distorted. This is primarily due to the shape and distribution of the detectors on the array and the location of the source being imaged. Figure 4.6 below depicts the differences that surface when $\Delta\phi$ is reintroduced. The image is a bit more noisy but still good enough to gather information about the sources being imaged.

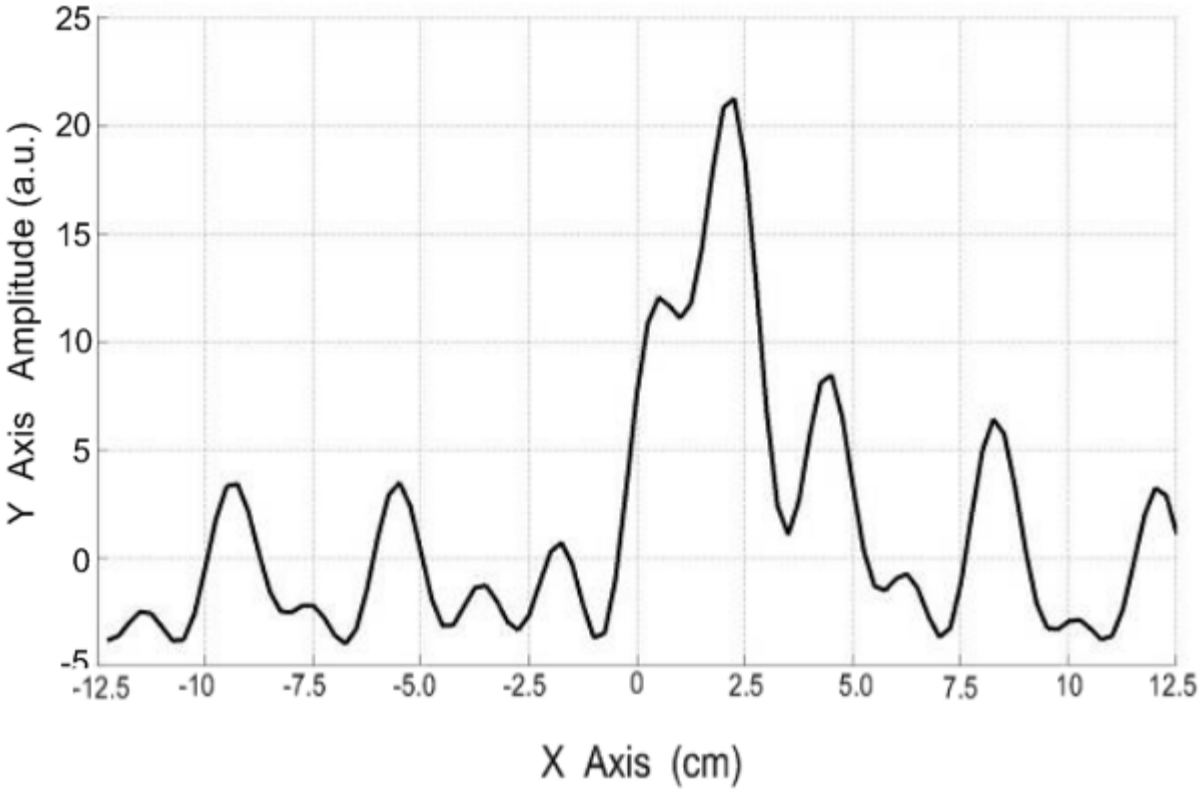

Figure 4.6: One dimensional 8 detector array image of Source A with non-zero $\Delta\phi$. Although the peak detected is no longer exactly at 50th data point, it is slightly offset due to array geometry and source location.

Another issue to take note of in Figure 4.6 above is the fact that other than the image being noisier and less symmetrical, the detected peak is slightly offset to the right. Originally the peak depicting the location of the source was exactly at the 50th data

point, however with $\Delta\phi$ non-zero, it is located closer to the 60th data point. This is primarily caused by the geometry and distribution of the array and the relative position of the source being imaged.

Next challenge to investigate with this setup is to try and detect 2 sources at the same time. Here the two sources are of equal magnitude with source A located at (0,0,1) and source B located at (0,0.08,1). The source B location translates to being 8cm to the right of source A. While imaging both sources A and B at the same time, it is necessary to account for the values of $\Delta\phi$. If $\Delta\phi$ was assumed to be zero, this would prevent the array from being able to detect the location of the second source. The magnitude detected in the middle of the array, at the 50th data point would be greater as it would roughly represent the contributions from both sources A and B according to the equation 4-7 above. Since $\Delta\phi$ is accounted for there is once again slight distortion from the exact location of the sources. Figure 4.7 below shows the scenario of detecting the two sources.

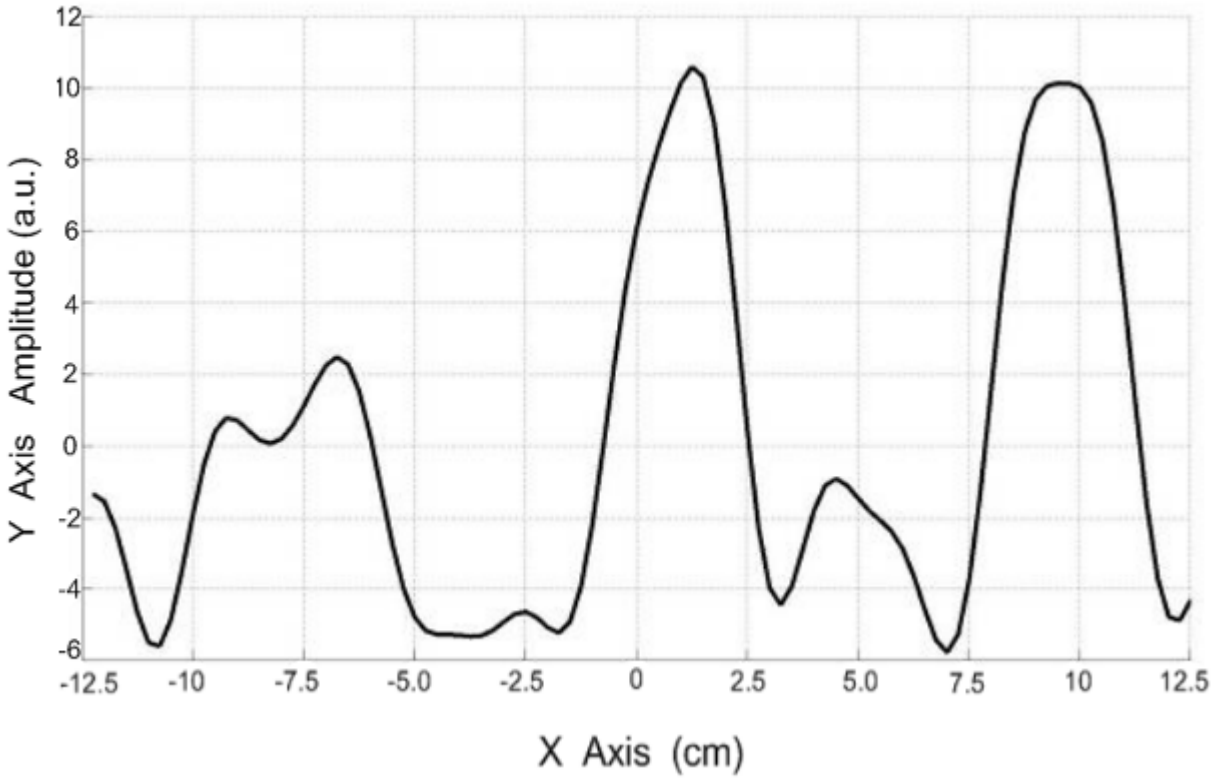

Figure 4.7: One dimensional 8 detector array image of source A located at (0,0,1) and source B located at (0,0.08,1) with non-zero values for $\Delta\phi$.

4.4 Two Dimensional Experiment

Once the one dimensional experiment was accomplished and verified it became clear that the work from [1] [2] [6] and [3] was properly followed. The next step was to match the two dimensional calculations and performance of their experiment. The first challenge in reproducing the experiment was coming up with a spiral array geometry that was similar to the spiral array used in the original experiment as no formula was given.

4.4.1 Theoretical Explanation

The first investigation into two dimensional imaging was to find out how to create a spiral array element pattern. The first candidate that was investigated was an Archimedean spiral followed by the second candidate, a logarithmic spiral.

The Archimedean spiral is characterized by the fact that the distances between successive turns of the spiral are constant. There are different ways to describe an Archimedean spiral, however below are the parametric equations that describe the Archimedean spiral used in this experiment in 4-11.

For t that goes from 1.5π to 4.5π…

$$\begin{aligned} x(t) &= (a)(t)\cos(t) \\ y(t) &= (a)(t)\sin(t) \end{aligned} \tag{4-11}$$

Where x and y are the Cartesian coordinates of the Archimedean spiral, a is a constant real number that determines the tightness of the winding. The two dimensional Archimedean spiral array used in this experiment is shown below in Figure 4.8

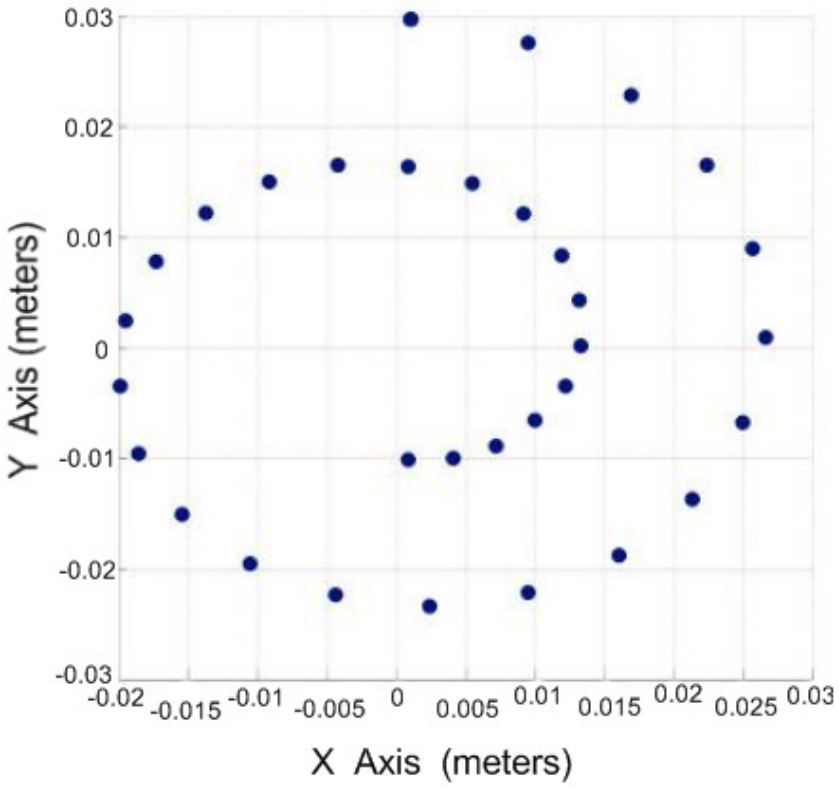

Figure 4.8: Two dimensional Archimedean spiral array used in this experiment.

Firstly the baselines for this array geometry must be recalculated. Since there are 32 detectors, there will be 32(32-1)/2 or 496 individual baselines, that is unique pairs of detectors. As with the one dimensional array scenario u_l as in $(x_n - x_m)$ and v_l as $(y_n - y_m)$ must be recalculated. Since in this scenario the array lies in the XY plane, v_l will have values, unlike in the one dimensional scenario.

In all simulations other than one dimensional scenario discussed earlier, the more complicated scenario with two sources rather than just one is used. The two sources unless noted otherwise are always the same. Source A is located at (0,0,0.96) meters with a magnitude of 1, and source B is located at (0.08,0,1.04) meters, also with a magnitude of 1. This yields a difference in distance along the Z axis between the sources of 8 cm.

Angular resolution is what determines the smallest discernable distance between two point sources. The angular resolution can be approximated as,

$$\theta_{\min} = \frac{\lambda}{b} \tag{4-12}$$

where θ_{min} is the minimum angular resolution, λ is the wavelength, and b is the maximum baseline in the array. [6] Taking into account the distance between the array and the sources being image, the lateral spatial resolution is,

$$\Delta L_{lat} = Z_0 \theta_{\min} = \frac{\lambda Z_0}{b} \tag{4-13}$$

where Z_0 is the distance between the array and the sources being imaged. [6] In the array geometry depicted in Figure 4.5 the maximum baseline is 5.64 cm. The frequency at which this imaging system operates is 0.3Thz, which corresponds to a wavelength of 1mm. With the distance from the detector array to the sources being an average of 1 meter, this yields a spatial resolution of about 2 cm.

The images that were generated by the simulation using the Archimedean spiral two dimensional arrays always yielded images similar to Figure 4.9 in that they depicted the two point sources being imaged in their expected locations and with the same intensity. This spiral array and simulation are excellent for imaging scenarios that attempt to image sources that are in the same plane, for example on the XY plane with similar Z values. This is because the results of the simulations with an Archimedean spiral array have not depicted a significantly discernable difference and sensitivity to differences in the Z direction between point sources. The simulation with the Archimedean spiral array has however demonstrated a very good ability to

detect two dimensional images of both two and three dimensional point source distributions.

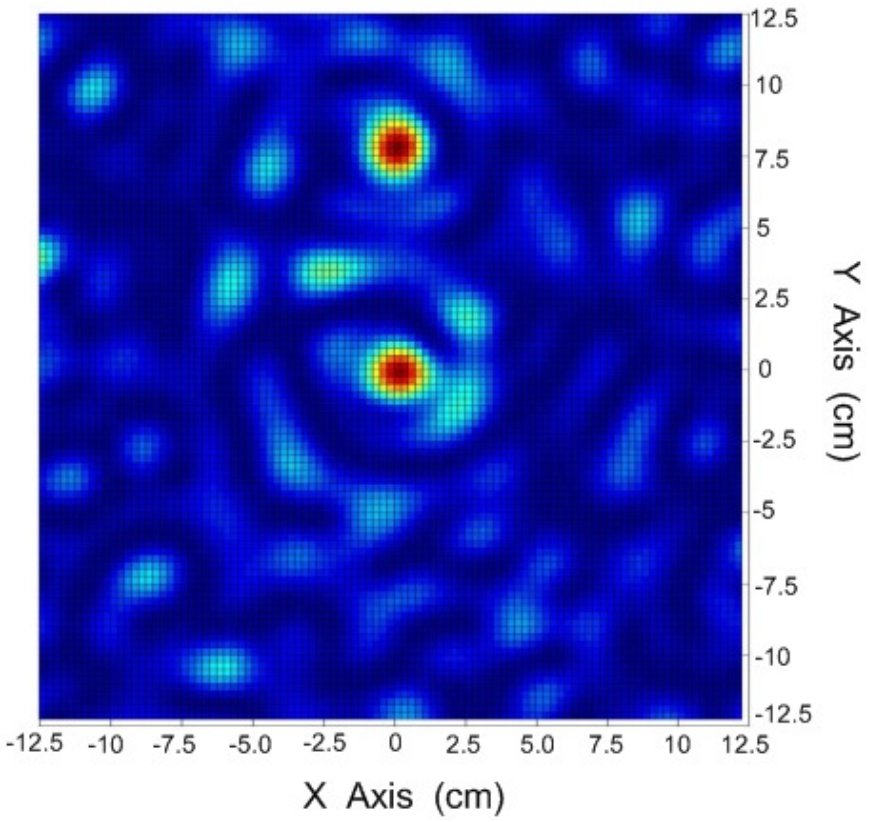

Figure 4.9: Two dimensional Archimedean spiral array showing source A located at (0,0,0.96) and source B located above at (0,0.08,1.04).

When simulations were done with sources in the same plane as well as sources that were a large distance apart in the Z direction the results seemed to be similar.

The Logarithmic spiral is characterized by the fact that any line projecting from the origin out, will intersect with the arm of the spiral forming the same angles. The Logarithmic spiral has many names and is extremely common in nature. The parametric equations for the Logarithmic spiral used in this experiment follows.

For *t* that goes from 2*π* to 5*π*…

$$x(t) = (a)e^{(b)(t)}\cos(t)$$
$$y(t) = (a)e^{(b)(t)}\cos(t) \qquad (4\text{-}14)$$

where *x* and *y* are the Cartesian coordinates of the Logarithmic spiral, *a* and *b* are constant real numbers that determine the tightness of the winding. The two dimensional Logarithmic array used in this experiments is depicted below in Figure 4.10

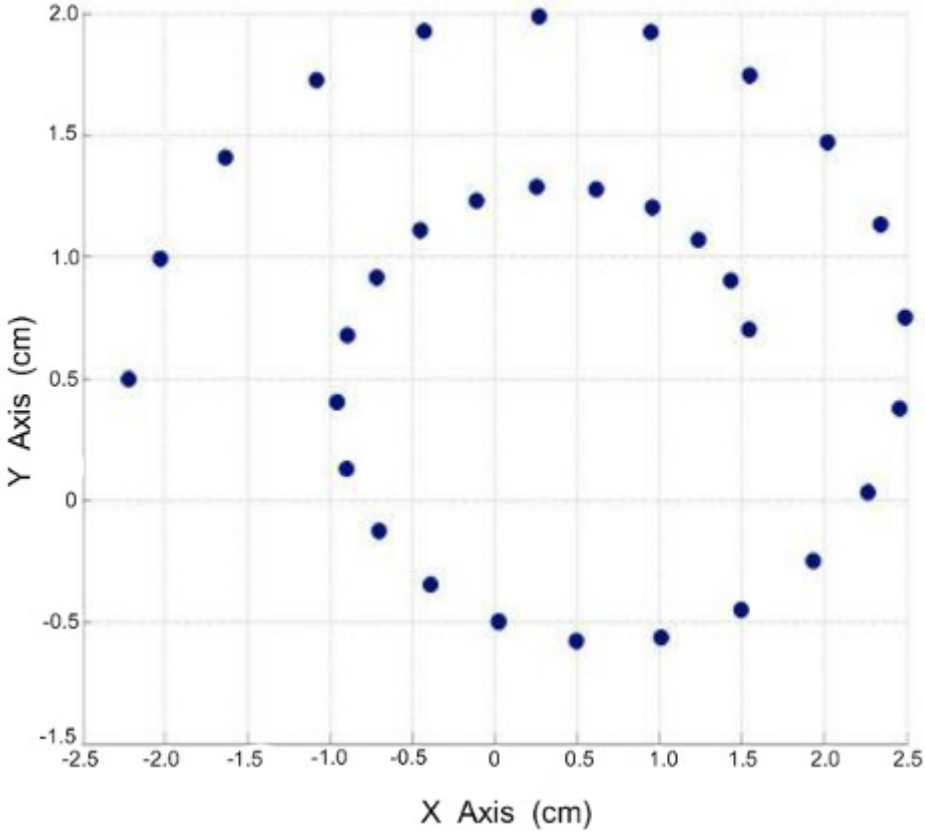

Figure 4.10: Two dimensional Logarithmic spiral array used in this experiment.

The Logarithmic spiral array used in this experiment also consists of 32 detector elements like the Archimedean spiral array discussed earlier. The sources images

with this array are identical in magnitude and location to those imaged with the Archimedean spiral array for consistency and comparison of results.

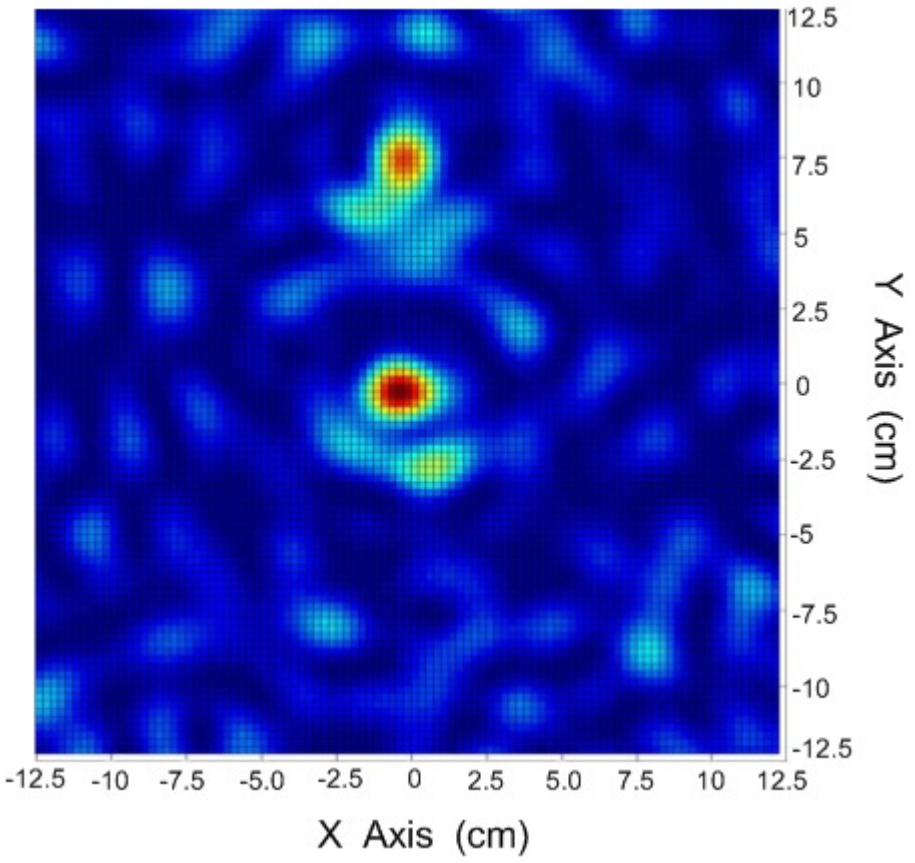

Figure 4.11: Image simulated with the Log Periodic or Logarithmic spiral array of the same two source A and B located at (0,0,0.96) and (0,0.08,1.04) respectively. Notice the difference between this and the Archimedean spiral array's image of the same sources under the same conditions. The Logarithmic array image shows source A more prominently than source B.

With the two dimensional Logarithmic spiral array it seems that depth perception or differentiation is better as the source that is nearer, namely source A, seems more prominent than the farther source B. In other simulations the results showed that the Log Periodic spiral array like the Archimedean spiral array cannot

detect a change in intensity between the sources as imaging is performed of planes at different planes. This is in contrast with the Archimedean spiral array that predominantly shows both sources to be of equal intensity. The Archimedean spiral array does show a difference in perceived intensity of two sources of equal intensity but at different distances from the source. It is vital to note that the differentiation in intensity detected by a Log Periodic spiral array is not proportional and doesn't change and you progress through the various imaging planes. Meaning that distance or source intensity information cannot be accurately inferred from the images. This highlights the major shortcoming of two dimensional imaging of this approach.

4.4.2 Simulation Results

Below are some images of the two dimensional array imaging two sources in Figure 4.12. These images show source A at (0,0,0.96) and source B at (0.04, 0, 1.04).

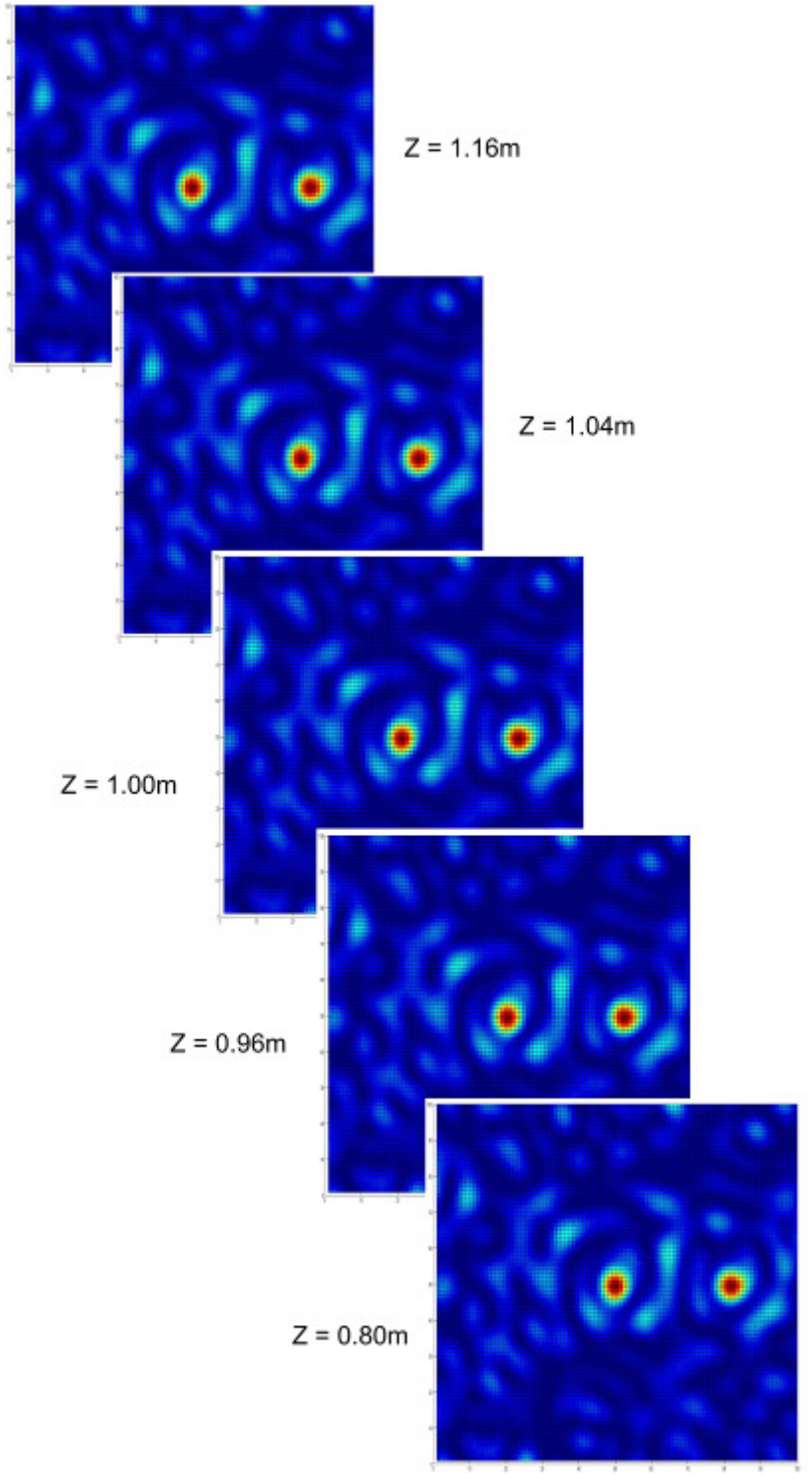

Figure 4.12: Five images of the two dimensional array imaging two sources. Z is the distance from the imaging array to the XY plane being imaged.

4.5 Three Dimensional Experiment

The next logical improvement on this imaging technique is to try and improve the depth perception of this system and to be able to obtain more information about the sources being imaged. It would be very useful and provide many new and interesting applications if it was possible to gather and generate three dimensional images of some source distributions. This two dimensional imaging approach generates a two dimensional image that is taken at a specific distance from the imaging array. To create a three dimensional image one approach that could be used is to obtain a series of two dimensional images taken at different distances from the imaging array that define a volume within which the sources reside. If this is done, then if the two dimensional images taken within the volume of the same two sources were slightly different, and showed the two sources waning and waxing in intensity depending on which sources is closer to the plane of the two dimensional image, then it would be possible to generate from the information contained in this series of two dimensional images a three dimensional image of the sources contained within the volume.

With the two dimensional simulation setup using the two dimensional spiral arrays, if we were to try and image a volume containing the two sources, the images at the various planes through the volume may show a changing variation in perceived intensity between the two sources at different distances from the imaging array, however these changes would not be proportional or accurate. To try and obtain more information about the source distribution and to be able to generate a better

three dimensional image a three dimensional array setup was proposed and examined.

4.5.1 Theoretical Explanation

For the three dimensional array simulation the equations are modified for the three dimensional scenario as described earlier in section 4.2. By extending the simulation to three dimensions it was thought to gain better depth perception from the array. Essentially it should simply provide another dimension in which there would be detectors placed at different distances thus allowing interferometric measurements to be taken in the third dimension.

To test this theory the two primary orientations that were tested earlier similar to Archimedean and Log Periodic spirals were used. In the third dimension a linear and a log periodic distribution was tested. This produced four different array geometries: Archimedean spiral with Linear depth, Archimedean spiral with Log Periodic depth, Log Periodic spiral with Linear depth, and Log Periodic spiral with Log Periodic depth. All four configurations were tested to try and figure out which one would work best and yield the most additional image information in three dimensions.

The approach for obtaining a three dimensional image is accomplished by taking a series of two dimensional images at consecutive points through a rectangular volume. These two dimensional images are images of the XY plane through the three dimensional volume that contains the sources, with Z values of the

plane going from 80 centimeters, at 84 centimeters, 88 centimeters, and so on until 120 centimeters from the imaging array. See Figure 4.13 below.

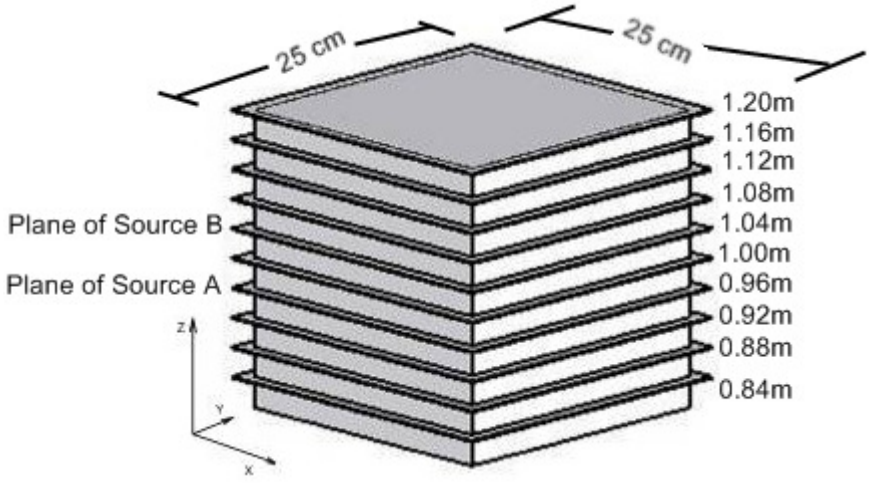

Figure 4.13: Diagram depicting the three dimensional volume that is being imaged in this experiment. This diagram also depicts the ten two dimensional cross sectional images taken at different Z values in the volume to collect three dimensional information.

Of the four configurations listed that were tested the results show that none of the Log Periodic spiral array configurations yielded results that were acceptable. All of the Log Periodic spiral arrays yielded results such that when imaging two sources, where one is nearer to the array while the other is farther away, as you progress through the ten equally spaced two dimensional images of the two sources taken at every 4 centimeters starting from 80 centimeters from the imaging array up to 120 centimeters; you do not see as you would hope the intensity of one source waxing and the other waning in perceived intensity.

The configurations that worked best had the Archimedean spiral configuration in the XY plane and a log periodic depth on the Z axis. These Archimedean spiral

arrays were best able to detect both sources and detect a difference in perceived intensity between them.

In the three dimensional experiment the Archimedean spiral arrays had a depth as well. The depth, or the array's projection on the Z axis was modeled as both linearly distributed, and log periodic. In the linearly distributed depth model each of the elements in the array were equally spaced out in the Z direction as depicted in Figure 4.14.

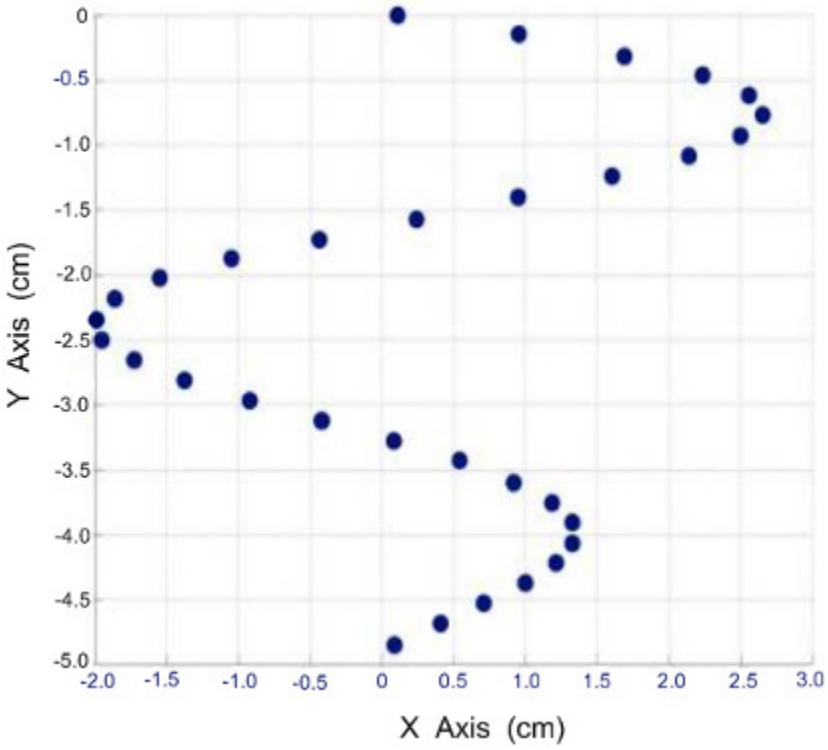

Figure 4.14: Linear distribution of elements of the three dimensional Archimedean spiral array shown in the XZ plane.

In the log periodic depth model each detector's Z value was increased in a logarithmic manner. The log periodic distribution of the array is depicted in Figure 4.15.

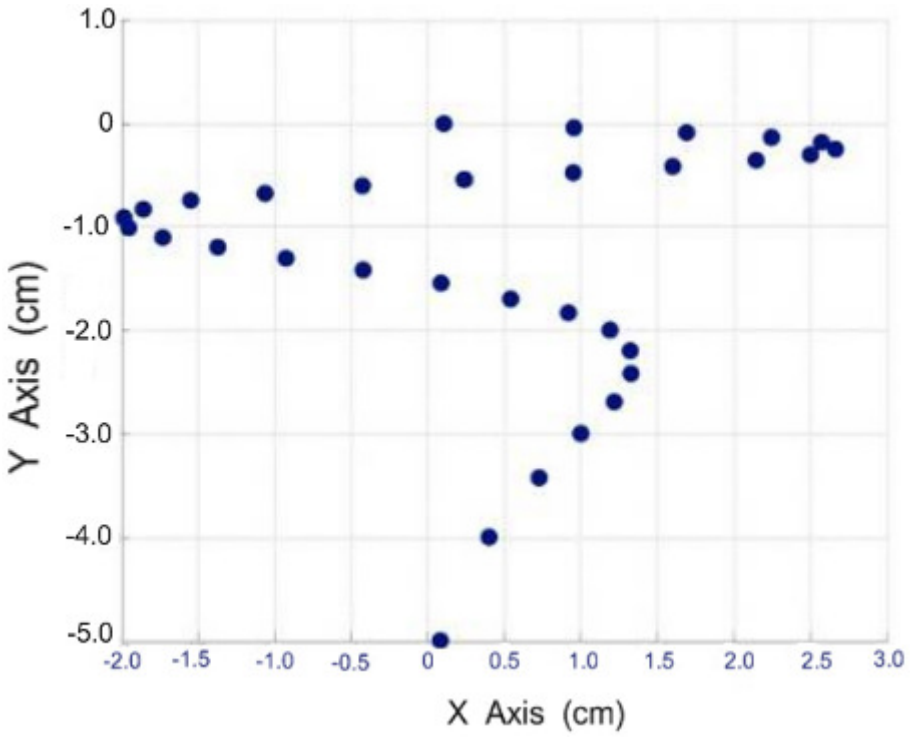

Figure 4.15: Log periodic distribution of elements of the three dimensional Archimedean spiral array shown in the XZ plane.

In the experiments that were modeled, the best results were received from using the log periodic depth pattern, and having the array with a depth of 0.05 meters. This made the spiral array roughly in the shape of an inverted cone as the diameter of the spiral was about 0.05 meters as well as the depth.

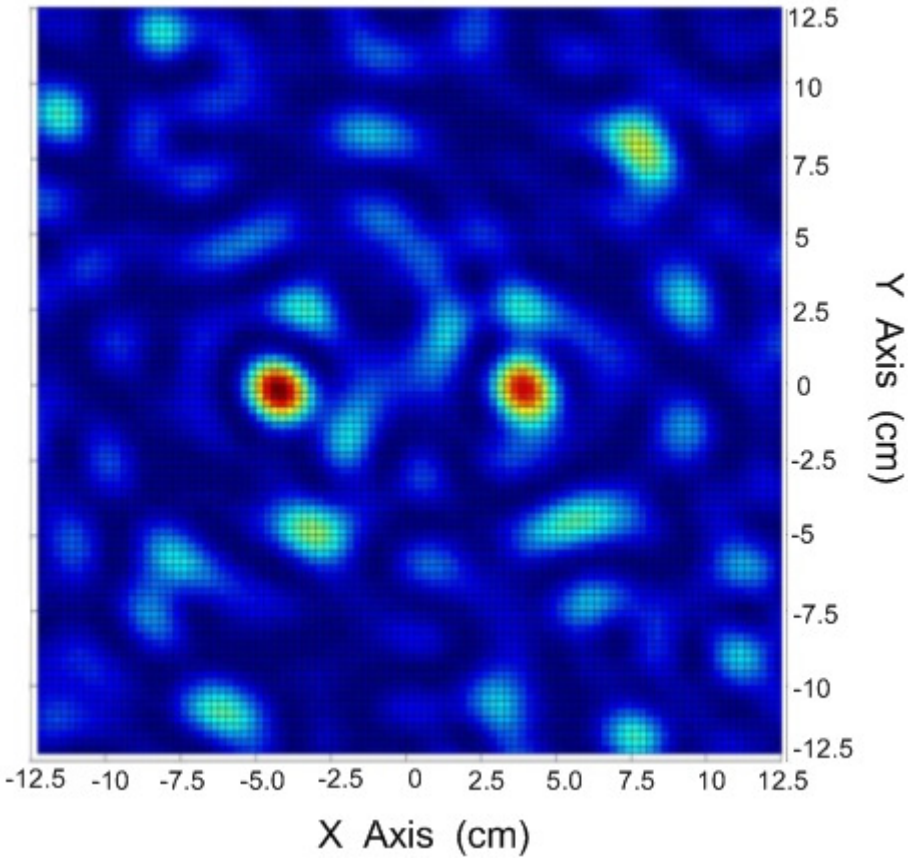

Figure 4.16: Two dimensional image of the two sources A and B located at A(-0.04,0,96) and B(0.04, 0, 1.04) mentioned earlier in this thesis in the two dimensional section taken at the imaging plane nearest to the imaging array.

The image above in Figure 4.16 is the two dimensional image taken within the volume depicted in Figure 4.13. This image shows the source on the left having a higher perceived intensity than the source on the right. The source on the left is located at 0.96 meters above the array whereas the source on the right is located at 1.04 meters above the array. If all ten two dimensional images were to be displayed, taken at each of the ten planes depicted in Figure 4.13, it would be clearly visible that with each image being taken farther from the imaging array the intensity of the source on the left would wane and the intensity of the source on the right would wax. This is

discussed in section 4.5.2 and demonstrated in Figure 4.18. The image in Figure 4.17 is the tenth image of the ten images depicted by planes in Figure 4.13. It is the image taken at the farthest distance from the imaging array. Being the farthest image, it shows the rightmost source as having more intensity than the left one since that image plane is closer to the right source.

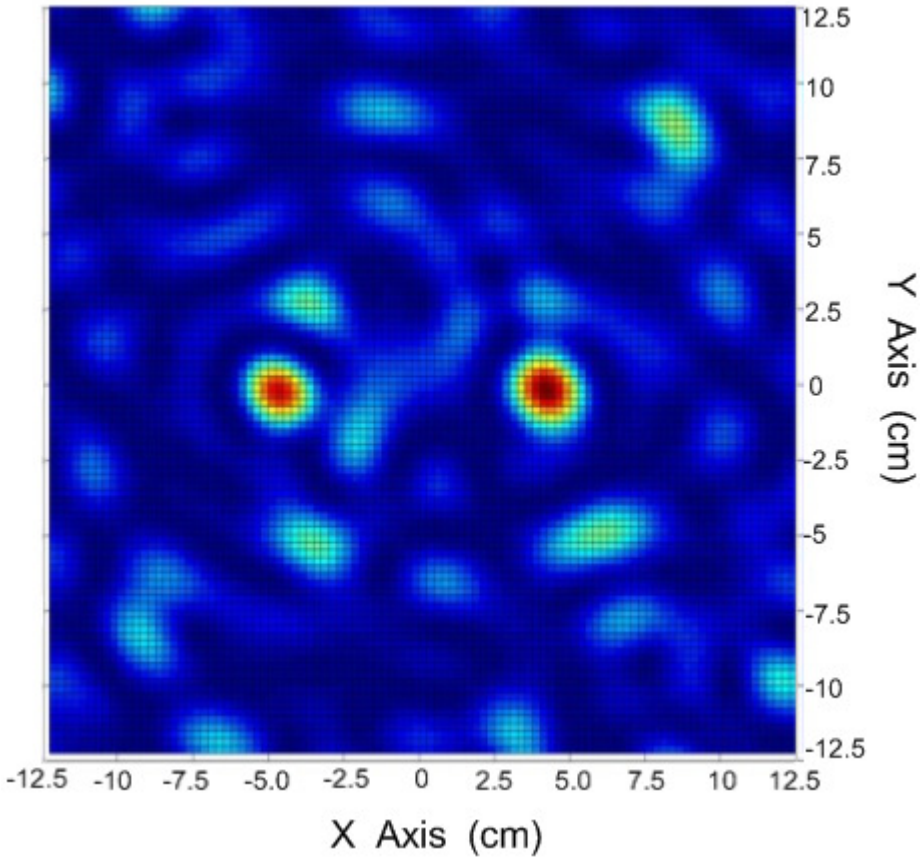

Figure 4.17: Image of the two sources A and B located at A(-0.04,0,96) and B(0.04, 0, 1.04) imaged with the array element distribution from Figure 4.15 in the farthest imaging plane from the array.

4.5.2 Simulation Results

Below are some images of the results from the three dimensional Archimedean spiral with linear depth array in Figure 4.18. These images show some

of the desired behavior hoped for. The two sources at different distances from the array are seen with different intensity depending on which XY plane is being measured.

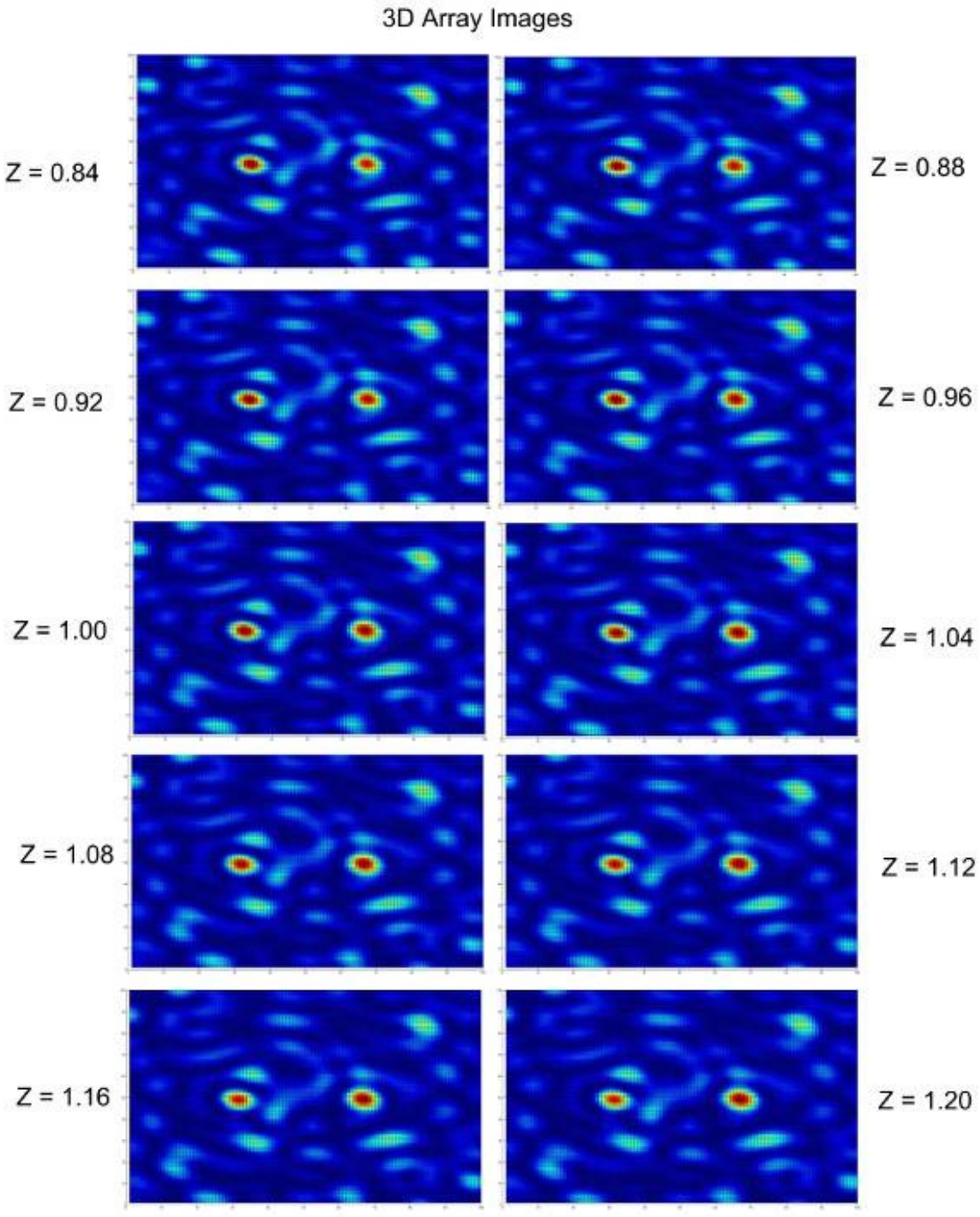

Figure 4.18: Three dimensional array images of two sources A (-0.04,0,0.96) and B (0.04,0,1.04)

4.6 Physical Experiment

After obtaining some hopeful results from the simulation it was possible to conduct an actual physical experiment of this concept with the help of David Wikner and Charles Dietlein from the Army Research Labs. We were able to use some of the resources of the Army Research Labs for the experiment.

There were some constraints and changes that needed to be made to adapt the simulated experiment to the equipment that was available. The Army Research Labs equipment required us to change the imaging frequency from 0.3Thz to 0.22Thz. This change required many other changes in dimensions of the experimental setup to keep all ratios the same. The dimensions of the array itself decreased a bit from about a 5cm diameter spiral in the XY plane to about 1.7cm, and the depth went from about 5cm to 2.5cm due to limitations of the detector articulation mechanism. The distance from the array to the sources was decreased from 1m to about 53.2cm.

4.6.1 Physical Experimental Setup

The Figure 4.19 below illustrates the physical experimental set up at the Army Research Labs. The Receiver in the diagram below (Figure 4.19) is mounted on an articulation mechanism that allows the receiver to slowly move and over-sample the magnitude and phase at data points with high granularity in a virtual three dimensional cube volume that encompasses the imaging array. From this data set of over-samples data, we were able to extract the data points that most closely resemble the simulated array data points. From the actual measurements obtained

from these select data points we were able to create images to be compared to the simulation images generated. The diagram below (Figure 4.19) shows the two sources located at virtually the same location. In the actual experiment the sources were located at the same location as well, however as the diagram shows, one of the sources has a longer wave guide which delays the phase of the signal simulating a different distance.

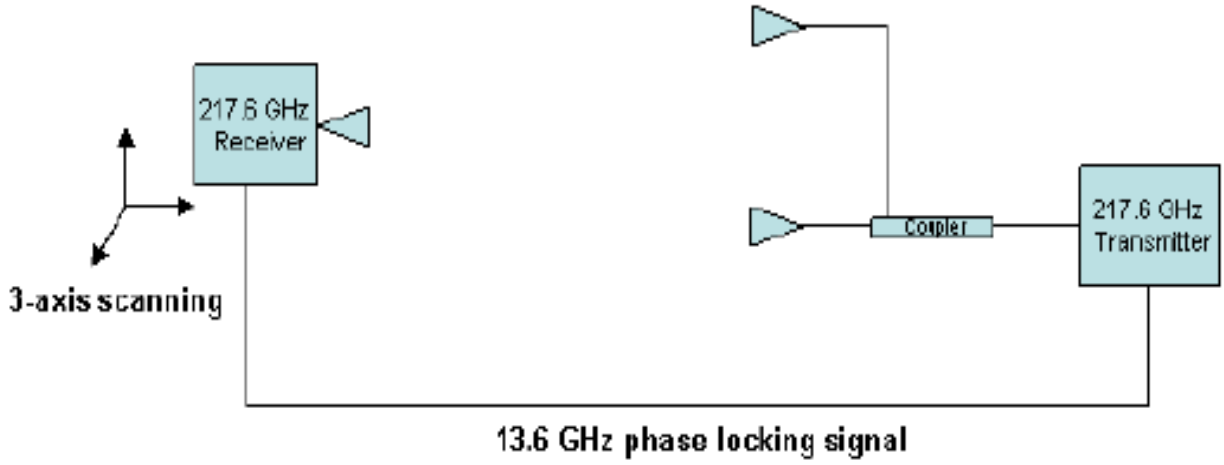

Figure 4.19: Simple representation of the physical experiment performed at the Army Research Labs. [7]

4.6.2 Physical Experiment Simulation Results

The results of the simulation of the experimental setup looked promising and seem to support the findings obtained in earlier experimentation. As theorized the closer source A on the left was more intense in the closer image planes and the right source B was more intense on the farthest image planes. However, the total intensity of the sources did keep growing and needs further investigation. The relative

intensity between the two sources did however show the desired waning and waxing effect. Figure 4.20 below shows the results of this simulation.

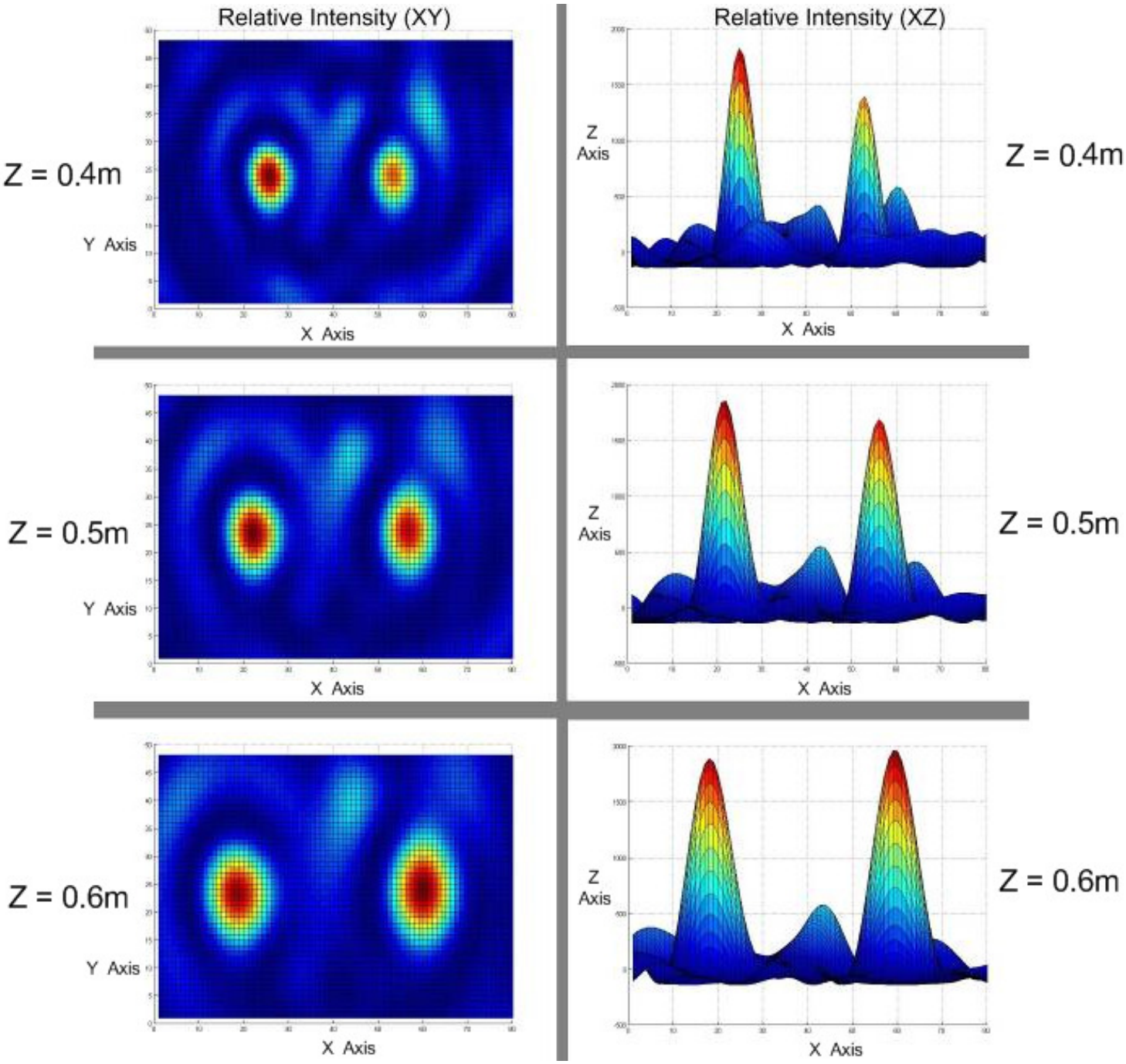

Figure 4.20: Comparison of the relative intensity between the two sources in the XY and XZ plane. Z is the distance from the imaging array in meters to the XY plane being imaged.

4.6.3 Physical Experiment Results

The results obtained from the physical experiment were reassuring and interesting. The analysis of the data showed that the simulations that were performed were accurate and on the right track. Both the two dimensional array and three dimensional array images produced good quality and accurate images of the two sources. The physical experiment results did however raise one point for further discussion and analysis. Unlike in the simulation of a two dimensional array where images at all 10 or so planes in the imaging volume were very similar in terms of the relative difference of intensity (Figure 4.12) between the two sources that were at different distances from the imaging array, in the physical experiment results the two dimensional array was able to do a decent job at discerning the intensity between the two sources. This is something that needs to be investigated further to determine if there is an error in the simulation logic or some inconsistency in the experimental setup. Starting from this initial work it should be possible to investigate if certain three dimensional array geometries may yield more spatial data that is useful to imaging sources in three dimensions.

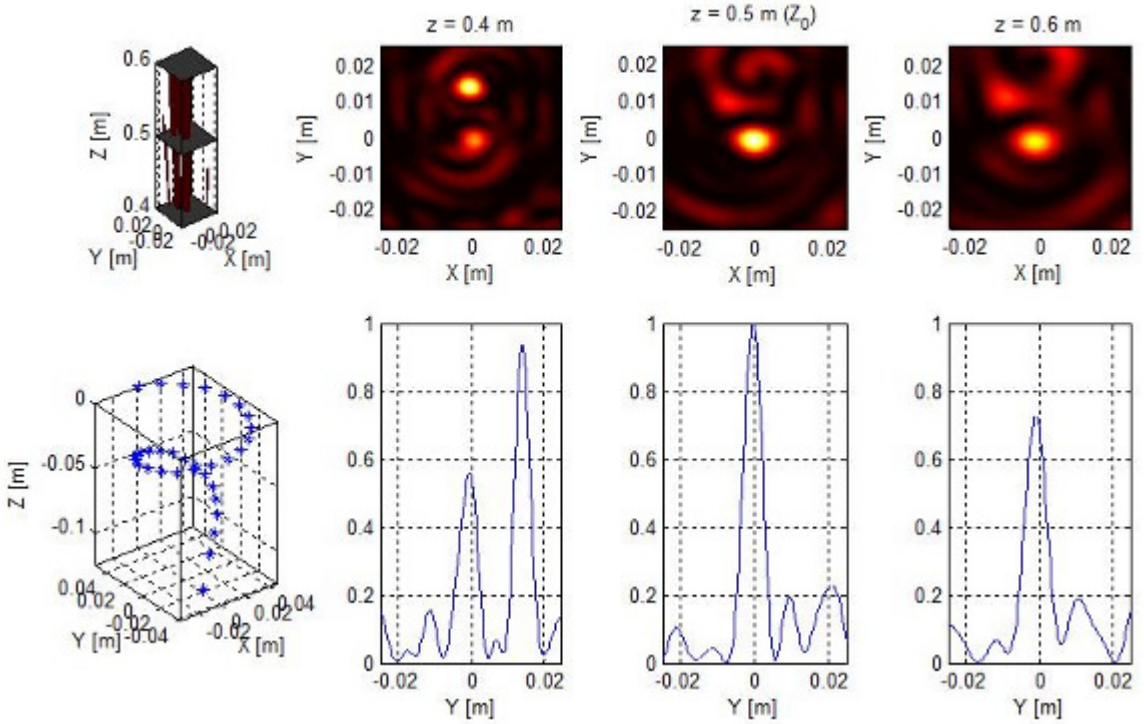

Figure 4.21: Three dimensional experiment results. [7]

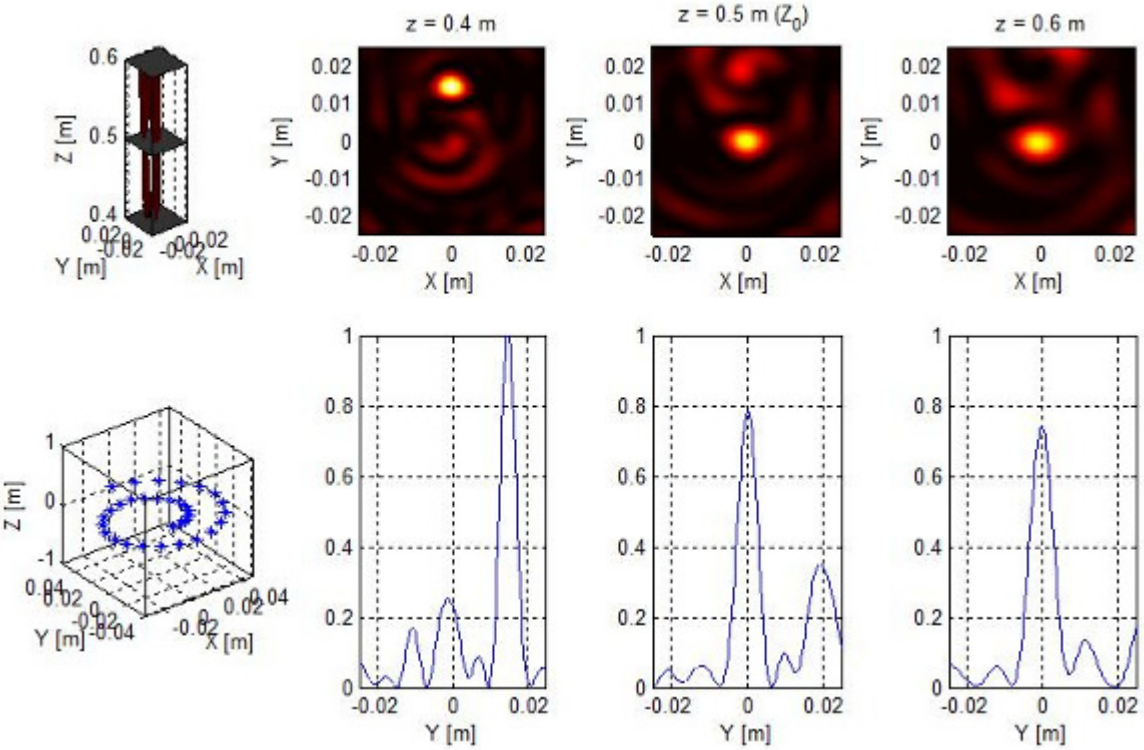

Figure 4.22: Two dimensional experiment results. [7]

Chapter 5: Conclusion

The three dimensional imaging technique discussed in this thesis has been demonstrated to operate successfully in that it can clearly detect a difference in perceived intensity between two sources of equal intensity located at different distances from the imaging array. The experimental setup investigated in this thesis produced a small flaw. As demonstrated in section 4.5 above the distance between the sources was 8 centimeters, which is somewhat large. In the array geometry depicted in Figure 4.15 the maximum baseline along the Z axis is 5 centimeters. Again, the frequency at which this imaging system operates is 0.3Thz, which corresponds to a wavelength of 1mm. With the distance from the detector array to the sources being an average of 1 meter, this yields a spatial resolution of 2 cm according to formula 4-13. According to these results for spatial resolution, the distinction in perceived intensity of two sources that are 8 centimeters apart should be not only clearly visible but should also be sharp enough where in the plane of one source; the second source is not even visible, or very dim in intensity. This flaw may be primarily due to the spiral orientation of this array as well as the number of baselines in the Z plane. It may be that for accurate measurement either more detectors are needed or more likely the distribution of those detectors in the Z plane may need to be redistributed or tweaked.

Even with the current resolution, perceived intensity can be used to allow measurement of the distance between sources. The very fact that additional, consistent, precise data can be collected from the three dimensional array

experiment demonstrated here compared with the two dimensional array experiment from the experiments in [1] [2] [3] and [6] is considerable and significant. This experimental simulation successfully demonstrates that this approach could be used to successfully image three dimensional scenarios.

5.1 Issues Identified and Areas for Further Research

There were some issues that were identified in the experimental data results. Further investigation of these issues may be helpful for better understanding of this interferometric imaging concept.

One issue that was noticed in both two dimensional and three dimensional array imaging that was performed was that as the successive image planes were examined, the exact position of the sources seemed to change and they seemed to drift apart. It was determined that this could be caused by the fact that the data points were collected as angular coordinates but plotted as Cartesian coordinates. This may contribute to the "drifting" effect that was observed in the images. Attempts to correct this issue by converting the coordinates by normalizing the expressions inside the Sin and Cos of equations 4-9 and 4-10 did not resolve the issue. In fact these corrections attempts seemed to disturb the images quite a bit and make them difficult to read. Attempts were made to normalize the components with various distances from end of array, start of array and middle of array to the sources. All attempts yielded similar results that degraded the images rather than helping. Correcting for incident wave curvature could perhaps help this as well. Resolving this "drifting" issue will make the images clearer and more consistent.

Another issue of concern that was identified was that for these simulation results although there was a visible difference in relative intensity between source A and B, the intensity would continue to grow as the imaging plane would move farther past the two sources. This behavior was not seen in the physical experimental data as seen in Figure 4.21. In the physical experiment simulation this change is not as pronounced as can be seen in figure 4.20 where the last imaging plane shows a stronger intensity in the right source, but the XZ profile image shows that the right source is only slightly more intense than the left source. There may need to be some further analysis of the simulation technique or determination of the source of the difference in the simulation.

Initially this experiment was started with a spiral array consisting of 64 detectors as in [2]. As the computations grew larger the computer hardware and even MATLAB were overwhelmed and would crash. It was necessary to scale down to using 32 detectors to allow the computer to calculate the equations. The other drawback was that each calculation took a long time on the hardware used. Depending on the simulation being run it would take from 30 minutes to over an hour to computer images for the volume. This is obviously impractical for real world applications, however with optimized hardware most of the time consuming calculations can be done in parallel, significantly reducing the calculation time required.

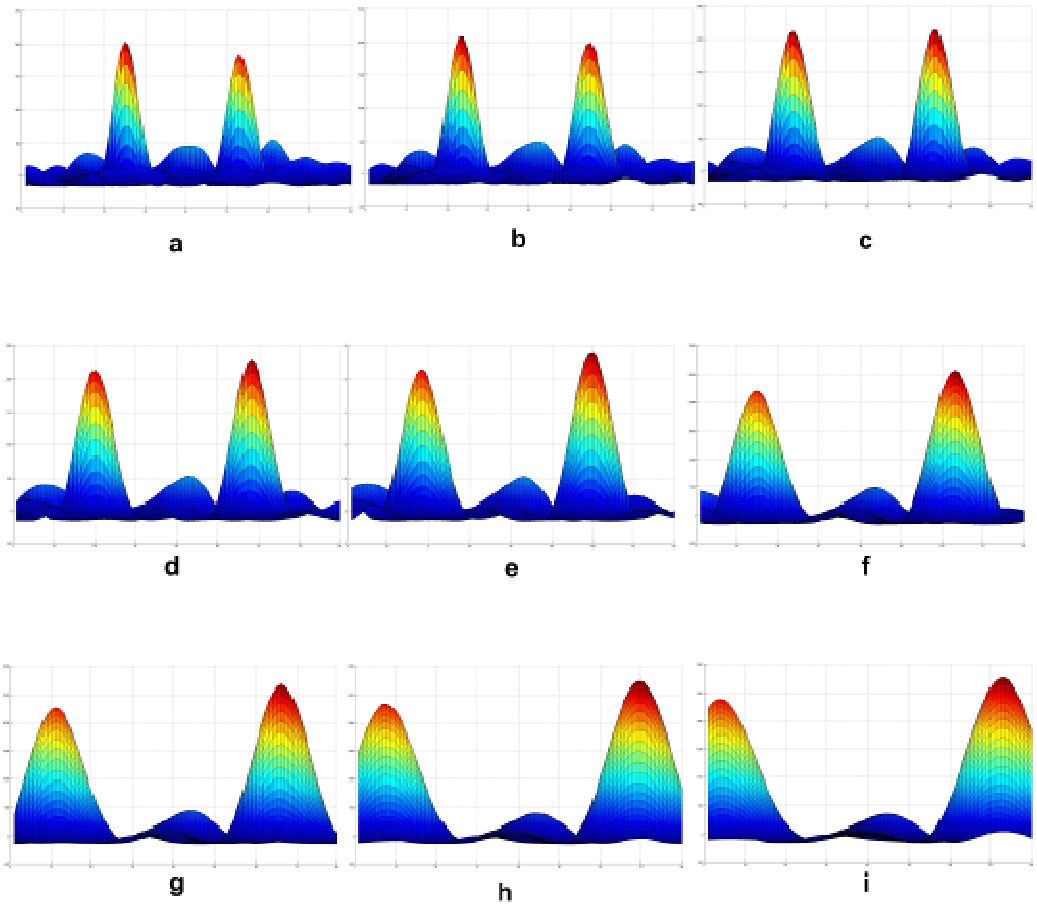

Figure 5.1: Progressive images showing the "drifting" effect of the location of the sources as well as the continued growth of the total intensity of the sources.

Another related aspect was that in the simulation of the two dimensional array the resulting images did not show a change in perceived relative intensity between the two sources as demonstrated in Figure 4.12. The relative intensity stayed constant throughout all the imaging planes. In the physical experiment even the two dimensional imaging showed good quality differentiation between the various imaging planes. Further investigation of this inconsistency would be helpful to better understand this experimental concept.

Appendix A: MATLAB Code

```
%*********************************************************************************
%
%       This file contains the commands and code for Matlab to calculate and
%       generate the simulation and images.
%
%       2/17/2009
%
%       Alex Goltsman
%
%*********************************************************************************

% The X and Y coordinates of all the array elements Log Periodic Spiral
arryX = [0.0104; 0.0093; 0.0073; 0.0046; 0.0012; -0.0025; -0.0061; -0.0095; -0.0122; -0.014; -0.0146; -0.0139; -0.012; -0.0089; -
0.0048; -0; 0.0051; 0.01; 0.0143; 0.0176; 0.0196; 0.0199; 0.0184; 0.0152; 0.0104; 0.0044; -0.0023; -0.0093; -0.0158; -0.0213; -
0.0253; -0.0272];

arryY = [0.004; 0.0079; 0.0114; 0.014; 0.0155; 0.0158; 0.0146; 0.0121; 0.0083; 0.0035; -0.0018; -0.0073; -0.0125; -0.0169; -
0.0201; -0.0216; -0.0213; -0.019; -0.015; -0.0093; -0.0025; 0.005; 0.0125; 0.0193; 0.0248; 0.0284; 0.0297; 0.0284; 0.0245;
0.0181; 0.0098; 0];

% The X and Y coordinates of all the array elements Archimedian Spiral
aryX = [0.0009; 0.0041; 0.0072; 0.01; 0.0122; 0.0133; 0.0132; 0.0119; 0.0092; 0.0055; 0.0009; -0.0042; -0.0092; -0.0137; -
0.0173; -0.0195; -0.0199; -0.0186; -0.0154; -0.0105; -0.0044; 0.0024; 0.0095; 0.016; 0.0214; 0.025; 0.0266; 0.0257; 0.0224;
0.0169; 0.0096; 0.0011];

aryY = [-0.0101; -0.01; -0.0088; -0.0066; -0.0035; 0.0002; 0.0043; 0.0084; 0.0121; 0.0148; 0.0164; 0.0166; 0.0151; 0.0122;
0.0078; 0.0024; -0.0035; -0.0096; -0.0151; -0.0195; -0.0224; -0.0233; -0.0221; -0.0188; -0.0136; -0.0068; 0.0009; 0.0089;
0.0165; 0.0229; 0.0275; 0.0297];

% Log Periodic Depth
arryZ = [];
for j=1:32 arryZ(j)=(log(j)-log(32))/log(32)*0.05; end

% Linear Depth
aryZ = [];
for j=1:32 aryZ(j) = (0 - j/32)*0.05; end

% Initialize the u, v, and w as the u-v field
u=zeros(1,496);
v=zeros(1,496);
w=zeros(1,496);

% All constant variables in simulation
deltaLAT = 0.0025;
f = 3e+011;                     % frequency
lambda = (3*10^8)/f;            % wavelength (f)
wavenum = (2*pi)/lambda;        % wavenumber (wavelength) aka "k"

% Calculate the u(l), v(l), and w(l).  These are essentially the various baselines
l = 1;
for j=1:31
for k=(j+1):32
v(l) = aryY(k)-aryY(j);
u(l) = aryX(k)-aryX(j);
w(l) = aryZ(k)-aryZ(j);
l = l + 1;
end
end

% Definition of any sources that will exist during the simulation
source1 = zeros(4,1); source1(1)=0; source1(2)=0.04; source1(3)=1.04; source1(4)=1;
source2 = zeros(4,1); source2(1)=0.03; source2(2)=0.035; source2(3)=1.00; source2(4)=1;
source3 = zeros(4,1); source3(1)=0; source3(2)=0; source3(3)=1.04; source3(4)=0;
source4 = zeros(4,1); source4(1)=0.08; source4(2)=0; source4(3)=0.96; source4(4)=0;
source5 = zeros(4,1); source25(1)=0; source25(2)=-0.04; source25(3)=0.96; source25(4)=1;
```

```
E_field_m=zeros((length(aryX)),1);        % initialization of array to hold the cumulative contribution from all the sources

for j=1:length(aryX)

% calculation to sum up the contributions from each source
E_field_m(j,1)=(source1(4)*exp(i*wavenum*sqrt(((aryX(j)-source1(1))^2)+((aryY(j)-source1(2))^2)+((aryZ(j)-
source1(3))^2))))/(sqrt(((aryX(j)-source1(1))^2)+((aryY(j)-source1(2))^2)+

((aryZ(j)-source1(3))^2)))+(source2(4)*exp(i*wavenum*sqrt(((aryX(j)-source2(1))^2)+((aryY(j)-source2(2))^2)+((aryZ(j)-
source2(3))^2))))/(sqrt(((aryX(j)-source2(1))^2)+((aryY(j)-

source2(2))^2)+((aryZ(j)-source2(3))^2)))+(source3(4)*exp(i*wavenum*sqrt(((aryX(j)-source3(1))^2)+((aryY(j)-
source3(2))^2)+((aryZ(j)-source3(3))^2))))/(sqrt(((aryX(j)-source3(1))^2)

+((aryY(j)-source3(2))^2)+((aryZ(j)-source3(3))^2)))+(source4(4)*exp(i*wavenum*sqrt(((aryX(j)-source4(1))^2)+((aryY(j)-
source4(2))^2)+((aryZ(j)-source4(3))^2))))/(sqrt(((aryX(j)-

source4(1))^2)+((aryY(j)-source4(2))^2)+((aryZ(j)-source4(3))^2)))+(source5(4)*exp(i*wavenum*sqrt(((aryX(j)-
source5(1))^2)+((aryY(j)-source5(2))^2)+((aryZ(j)-source5(3))^2))))/(sqrt

(((aryX(j)-source5(1))^2)+((aryY(j)-source5(2))^2)+((aryZ(j)-source5(3))^2)))+(source6(4)*exp(i*wavenum*sqrt(((aryX(j)-
source6(1))^2)+((aryY(j)-source6(2))^2)+((aryZ(j)-source6(3))

^2))))/(sqrt(((aryX(j)-source6(1))^2)+((aryY(j)-source6(2))^2)+((aryZ(j)-
source6(3))^2)))+(source7(4)*exp(i*wavenum*sqrt(((aryX(j)-source7(1))^2)+((aryY(j)-source7(2))^2)+((aryZ(j)-

source7(3))^2))))/(sqrt(((aryX(j)-source7(1))^2)+((aryY(j)-source7(2))^2)+((aryZ(j)-
source7(3))^2)))+(source8(4)*exp(i*wavenum*sqrt(((aryX(j)-source8(1))^2)+((aryY(j)-source8(2))^2)

+((aryZ(j)-source8(3))^2))))/(sqrt(((aryX(j)-source8(1))^2)+((aryY(j)-source8(2))^2)+((aryZ(j)-
source8(3))^2)))+(source9(4)*exp(i*wavenum*sqrt(((aryX(j)-source9(1))^2)+((aryY(j)-

source9(2))^2)+((aryZ(j)-source9(3))^2))))/(sqrt(((aryX(j)-source9(1))^2)+((aryY(j)-source9(2))^2)+((aryZ(j)-
source9(3))^2)))+(source10(4)*exp(i*wavenum*sqrt(((aryX(j)-source10(1))

^2)+((aryY(j)-source10(2))^2)+((aryZ(j)-source10(3))^2))))/(sqrt(((aryX(j)-source10(1))^2)+((aryY(j)-source10(2))^2)+((aryZ(j)-
source10(3))^2)))+(source11(4)*exp(i*wavenum*sqrt

(((aryX(j)-source11(1))^2)+((aryY(j)-source11(2))^2)+((aryZ(j)-source11(3))^2))))/(sqrt(((aryX(j)-source11(1))^2)+((aryY(j)-
source11(2))^2)+((aryZ(j)-source11(3))^2)))+(source12(4)

*exp(i*wavenum*sqrt(((aryX(j)-source12(1))^2)+((aryY(j)-source12(2))^2)+((aryZ(j)-source12(3))^2))))/(sqrt(((aryX(j)-
source12(1))^2)+((aryY(j)-source12(2))^2)+((aryZ(j)-source12(3))

^2)))+(source13(4)*exp(i*wavenum*sqrt(((aryX(j)-source13(1))^2)+((aryY(j)-source13(2))^2)+((aryZ(j)-
source13(3))^2))))/(sqrt(((aryX(j)-source13(1))^2)+((aryY(j)-source13(2))^2)+

((aryZ(j)-source13(3))^2)))+(source14(4)*exp(i*wavenum*sqrt(((aryX(j)-source14(1))^2)+((aryY(j)-source14(2))^2)+((aryZ(j)-
source14(3))^2))))/(sqrt(((aryX(j)-source14(1))^2)+((aryY

(j)-source14(2))^2)+((aryZ(j)-source14(3))^2)))+(source15(4)*exp(i*wavenum*sqrt(((aryX(j)-source15(1))^2)+((aryY(j)-
source15(2))^2)+((aryZ(j)-source15(3))^2))))/(sqrt(((aryX(j)-

source15(1))^2)+((aryY(j)-source15(2))^2)+((aryZ(j)-source15(3))^2)))+(source16(4)*exp(i*wavenum*sqrt(((aryX(j)-
source16(1))^2)+((aryY(j)-source16(2))^2)+((aryZ(j)-source16(3))

^2))))/(sqrt(((aryX(j)-source16(1))^2)+((aryY(j)-source16(2))^2)+((aryZ(j)-
source16(3))^2)))+(source17(4)*exp(i*wavenum*sqrt(((aryX(j)-source17(1))^2)+((aryY(j)-source17(2))^2)+

((aryZ(j)-source17(3))^2))))/(sqrt(((aryX(j)-source17(1))^2)+((aryY(j)-source17(2))^2)+((aryZ(j)-
source17(3))^2)))+(source18(4)*exp(i*wavenum*sqrt(((aryX(j)-source18(1))^2)+((aryY

(j)-source18(2))^2)+((aryZ(j)-source18(3))^2))))/(sqrt(((aryX(j)-source18(1))^2)+((aryY(j)-source18(2))^2)+((aryZ(j)-
source18(3))^2)))+(source19(4)*exp(i*wavenum*sqrt(((aryX(j)-

source19(1))^2)+((aryY(j)-source19(2))^2)+((aryZ(j)-source19(3))^2))))/(sqrt(((aryX(j)-source19(1))^2)+((aryY(j)-
source19(2))^2)+((aryZ(j)-source19(3))^2)))+(source20(4)*exp
```

```
(i*wavenum*sqrt(((aryX(j)-source20(1))^2)+((aryY(j)-source20(2))^2)+((aryZ(j)-source20(3))^2)))/(sqrt(((aryX(j)-
source20(1))^2)+((aryY(j)-source20(2))^2)+((aryZ(j)-source20(3))

^2)))+(source21(4)*exp(i*wavenum*sqrt(((aryX(j)-source21(1))^2)+((aryY(j)-source21(2))^2)+((aryZ(j)-
source21(3))^2))))/(sqrt(((aryX(j)-source21(1))^2)+((aryY(j)-source21(2))^2)+

((aryZ(j)-source21(3))^2)))+(source22(4)*exp(i*wavenum*sqrt(((aryX(j)-source22(1))^2)+((aryY(j)-source22(2))^2)+((aryZ(j)-
source22(3))^2))))/(sqrt(((aryX(j)-source22(1))^2)+((aryY

(j)-source22(2))^2)+((aryZ(j)-source22(3))^2)))+(source23(4)*exp(i*wavenum*sqrt(((aryX(j)-source23(1))^2)+((aryY(j)-
source23(2))^2)+((aryZ(j)-source23(3))^2))))/(sqrt(((aryX(j)-

source23(1))^2)+((aryY(j)-source23(2))^2)+((aryZ(j)-source23(3))^2)))+(source24(4)*exp(i*wavenum*sqrt(((aryX(j)-
source24(1))^2)+((aryY(j)-source24(2))^2)+((aryZ(j)-source24(3))

^2))))/(sqrt(((aryX(j)-source24(1))^2)+((aryY(j)-source24(2))^2)+((aryZ(j)-
source24(3))^2)))+(source25(4)*exp(i*wavenum*sqrt(((aryX(j)-source25(1))^2)+((aryY(j)-source25(2))^2)+

((aryZ(j)-source25(3))^2))))/(sqrt(((aryX(j)-source25(1))^2)+((aryY(j)-source25(2))^2)+((aryZ(j)-source25(3))^2)));
E_field(j,1)=(MagA*exp(i*wavenum*sqrt((aryX(j)^2)+(aryY(j)^2)+

((aryZ(j))-(sourceA(3)))^2)))/(sqrt((aryX(j)^2)+(aryY(j)^2)+((aryZ(j))-(sourceA(3)))^2))+(MagB*exp(i*wavenum*sqrt(((aryX(j)-
sourceB(1))^2)+((aryY(j)-sourceB(2))^2)+((aryZ(j)-sourceB

(3))^2))))/(sqrt(((aryX(j)-sourceB(1))^2)+((aryY(j)-sourceB(2))^2)+((aryZ(j)-sourceB(3))^2)));
end

l = 1;

E_field_mag_baseline=zeros(1,(length(u)));          % initializes the array of baselines

for j=1:31
for k=(j+1):32
E_field_mag_baseline(l) = abs(E_field_m(k)) * abs(E_field_m(j));          % calculates all the baselines
l = l + 1;
end
end

phase=zeros((length(aryX)),1);                          % initializes the array for the phase recorded at each detector

for j=1:length(aryX)
phase(j,1)=angle(E_field_m(j));                          % caluculates the phase recorded at each detector
end

delta_phase=zeros((length(u)),1);          % initializes the difference in phase in a baseline

l = 1;

for j=1:31
for k=(j+1):32
delta_phase(l) = phase(k) - phase(j);      % calculates the difference in phase in a baseline
l = l + 1;
end
end

deltaLAT = 0.0025;  % multiplier of the true minimum delta lateral displacement actual is = lambda/(max baseline)

l = 0;

Sigma = zeros(1,496);            % initialization of array to calculate the sigma calculation

Image = zeros(round(.25/deltaLAT),round(.25/deltaLAT),round(.4/(16*deltaLAT)));                          % initialization of array to
hold the cumulative image data

% loop to iterate through every "pixel" of the full image array
for j=1:round(.25/deltaLAT)
for k=1:round(.25/deltaLAT)
for m=1:round(.4/(16*deltaLAT))
l = 1;
```

```
% loop to actually calculate the sigma calcaltion and sum up the sigma commands in the image array
for r=1:31
for s=(r+1):32

% sigma calculation
Sigma(l)=real(E_field_mag_baseline(l)*exp(i*delta_phase(l)))*cos(wavenum*(((aryX(s)*(-0.125+j*deltaLAT)/((1+m*4*deltaLAT)-
aryZ(s)))-(aryX(r)*(-0.125+j*deltaLAT)/((1+m*4*deltaLAT)-

aryZ(r))))+((aryY(s)*(-0.125+k*deltaLAT)/((1+m*4*deltaLAT)-aryZ(s)))-(aryY(r)*(-0.125+k*deltaLAT)/((1+m*4*deltaLAT)-
aryZ(r))))+((aryZ(s)*(1+m*4*deltaLAT)/((1+m*4*deltaLAT)-aryZ(s)))

-(aryZ(r)*(1+m*4*deltaLAT)/((1+m*4*deltaLAT)-aryZ(r))))))-
imag(E_field_mag_baseline(l)*exp(i*delta_phase(l)))*sin(wavenum*(((aryX(s)*(-0.125+j*deltaLAT)/((1+m*4*deltaLAT)-aryZ(s)))-

(aryX(r)*(-0.125+j*deltaLAT)/((1+m*4*deltaLAT)-aryZ(r))))+((aryY(s)*(-0.125+k*deltaLAT)/((1+m*4*deltaLAT)-aryZ(s)))-
(aryY(r)*(-0.125+k*deltaLAT)/((1+m*4*deltaLAT)-aryZ(r))))+((aryZ

(s)*(1+m*4*deltaLAT)/((1+m*4*deltaLAT)-aryZ(s)))-(aryZ(r)*(1+m*4*deltaLAT)/((1+m*4*deltaLAT)-aryZ(r))))));

% image array summary
Image(j,k,m)=Image(j,k,m) + Sigma(l);
l = l + 1;
end
end
end
end
end

% Show the two dimentional images at various elevations
surf(Image(:,:,1)); view(2);
surf(Image(:,:,2)); view(2);
surf(Image(:,:,3)); view(2);
surf(Image(:,:,4)); view(2);
surf(Image(:,:,5)); view(2);
surf(Image(:,:,6)); view(2);
surf(Image(:,:,7)); view(2);
surf(Image(:,:,8)); view(2);
surf(Image(:,:,9)); view(2);
surf(Image(:,:,10)); view(2);


% This section of code traverses the Image matrix and extracts the data about where the max values occure

DataES = [0.0; 0.0; 0.0; 0.0; 0.0; 0.0; 0.0; 0.0; 0.0; 0.0];        % stores the max values at each elevation
BigHigh = [0.0;0.0;0.0;0.0];     % "cursor" that iterates through Image matrix
highA = [0.0;0.0;0.0;0.0];       % stores the max intensity of the left source
highB = [0.0;0.0;0.0;0.0];       % stores the max intensity of the right source

% loop to iterate through Image matrix and find the maxes
for m=1:10
for j=1:100
for k=1:100
if (Data(j,k,m) > BigHigh(4))
BigHigh(1)=j; BigHigh(2)=k; BigHigh(3)=m; BigHigh(4)=Data(j,k,m);
end
end
end

% storing the maxes in an array
DataX(m)=BigHigh(1); DataY(m)=BigHigh(2); DataES(m)=BigHigh(4);
if (BigHigh(2) < 55)
highA = BigHigh;
end
if (BigHigh(2) > 55)
highB = BigHigh;
end
end

% command to display the max at each level of the image matrix
                                        scatter3(DataX,DataY,DataZ,DataES,DataC,'filled');
```

Appendix B: Excerpt from John D. Kraus's "Radio Astronomy" Reproduced from reference [5] with permission.

B.1 The Simple (Adding) Interferometer

The resolution of a radio telescope can be improved, for example, by increasing the aperture *a*. However, this may not be economically feasible. A less expensive approach to the problem is to use two antennas spaced a distance *s* apart, as in Fig 3.1. If each antenna has a uniform aperture distribution of width *a*, the resulting autocorrelation function is as shown in Fig B.2.

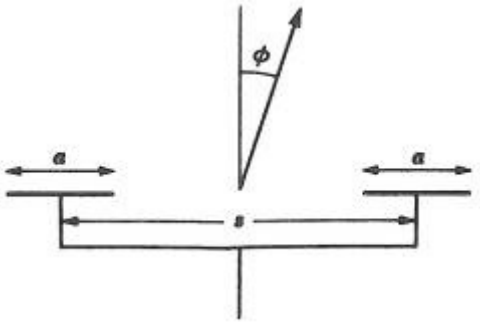

Figure B.1: Simple Interferometer.

It is apparent that by making observations with spacing out to s_λ it is possible to obtain higher spatial-frequency components in the observed pattern to a cutoff

$$\chi_{\lambda_c} = s_\lambda + \alpha_\lambda \qquad \text{(Y-1)}$$

and a smaller resolution angle

(Y-2)

$$\phi_c = \frac{1}{s_\lambda + \alpha_\lambda} rad = \frac{57.3}{s_\lambda + \alpha_\lambda} \deg$$

In the following analysis it will be shown that if observations are made to sufficiently large spacing, it is possible, in principle, to deduce the true brightness distribution.

The normalized far-field pattern of the two-element array from [a previous example] is

$$E(\phi) = E_n(\phi)\cos\left(\frac{\psi}{2}\right) \qquad \text{(Y-3)}$$

where $E_n(\phi)$ is the normalized field patter of an individual array element and $\psi = 2\pi s_\lambda \sin \phi$. The relative power pattern is equal to the square of $|E(\phi)|$, or

$$P(\phi) = \left|E(\phi)\right|^2 = \left|E_n(\phi)\right|^2 \cos^2 \frac{\psi}{2} = \frac{\left|E_n(\phi)\right|^2 (1+\cos\psi)}{2} \qquad \text{(Y-4)}$$

For large spacing the pattern has many lobes, which, in optics, are referred to as fringes. The first null occurs when $\psi = \pi$, from which the beam width between first nulls, or *fringe spacing*, is

$$BWFN = \frac{1}{s_\lambda} rad = \frac{57.3}{s_\lambda} \deg \qquad \text{(Y-5)}$$

This is one-half the BWFN value for a continuous array of aperture width $a_\lambda = s_\lambda$ or a large array of discrete sources of the same length ($L_\lambda = s_\lambda$) as given by [previous example].

The pattern maxima occur when $\psi = 2\pi n$, where n (= 0, 1, 2, 3,…) is the *fringe order*. Thus

$$\phi_{\max} = \frac{n}{s_\lambda} rad = \frac{57.3n}{s_\lambda} \deg \qquad \text{(Y-6)}$$

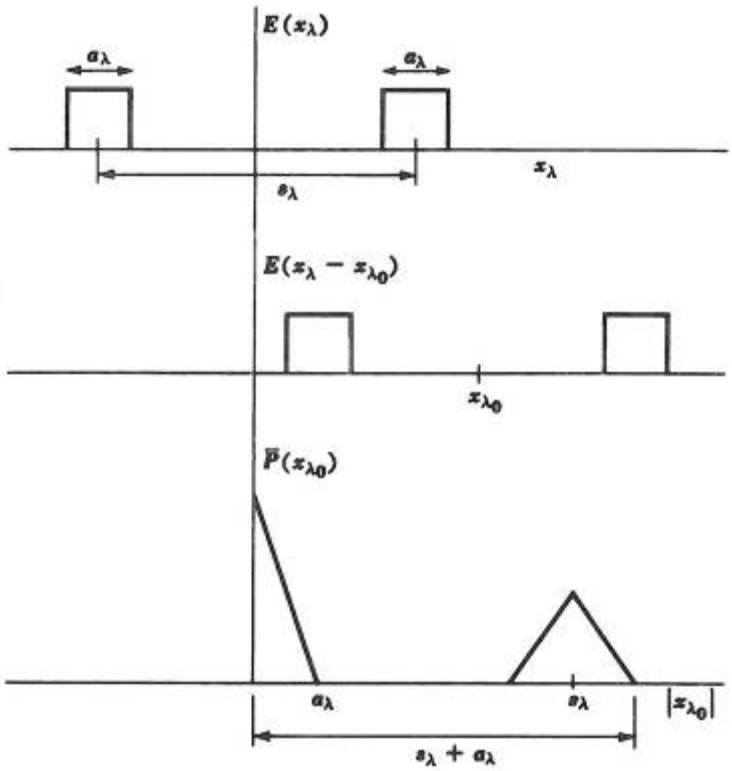

Figure B.2: Autocorrelation function of aperture distribution of simple interferometer.

Referring to Fig B.3, the first factor in (Y-4) represents the individual element pattern, as shown in (*a*), and the second factor the pattern of the array of two elements, as in (*b*). The product of the two factors gives the interferometer pattern, as indicated in (*c*). In these patterns a point source is implied. In the general case, for a source of angular extent α the observed flux density is the convolution of the true source distribution and the antenna power pattern, as discussed in [an earlier example]. Assuming the source extent is small compared to the individual element pattern, so that $|E_n(\phi)|$ is essentially constant across the source, we have in the one dimensional case that

$$S(\phi_0, s_\lambda) = |E_n(\phi)|^2 \int_{-\alpha/2}^{+\partial/2} B(\phi)\{1 + \cos[2\pi s_\lambda \sin(\phi_0 - \phi)]\}d\phi$$
$$S(\phi_0, s_{\lambda)} = |E_n(\phi)|^2 \left\{S_0 + \int_{-\alpha/2}^{+\alpha/2} B(\phi)\cos[2\pi s_\lambda \sin(\phi_0 - \phi)]d\phi\right\} \qquad \text{(Y-7)}$$

where $S(\phi_0, s_\lambda)$ = observed flux density distribution, watts $m^{-2}H^{-1}$, $B(\phi)$ = true source brightness distribution, watts $m^{-2}Hz^{-1}$ sr^{-1}, ϕ_0 = displacement angle in rad, α = source extent in rad, $s_\lambda = s/\lambda$ where s is interferometer element spacing, S_0 = flux density of source.

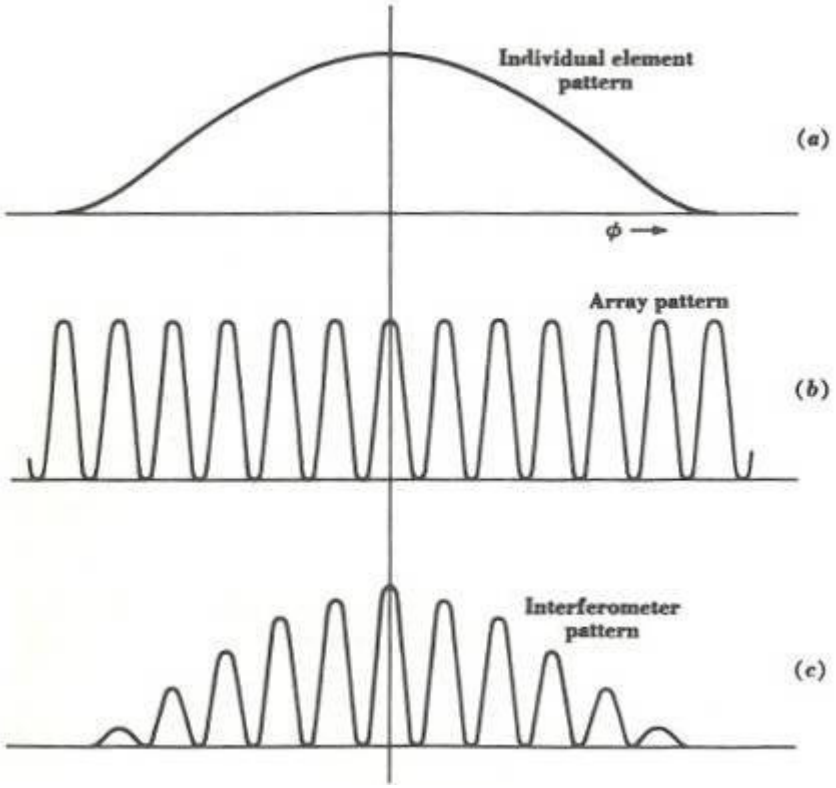

Figure B.3: (a) Individual element pattern; (b) array pattern; and (c) the resultant interferometer pattern for the case of a point source

The observed distribution as a function of hour angle is shown in Fig. B.4 for three cases: Fig. B.4a, source extent very small compared with lobe spacing ($\alpha << 1/s_\lambda$), the same as in Fig. B.3; Fig. B.4b, source extent comparable to, but smaller than, the lobe spacing ($\alpha < 1/s_\lambda$); and Fig. B.4c, source distribution uniform and equal in extent to the lobe spacing ($\alpha = 1/s_\lambda$).

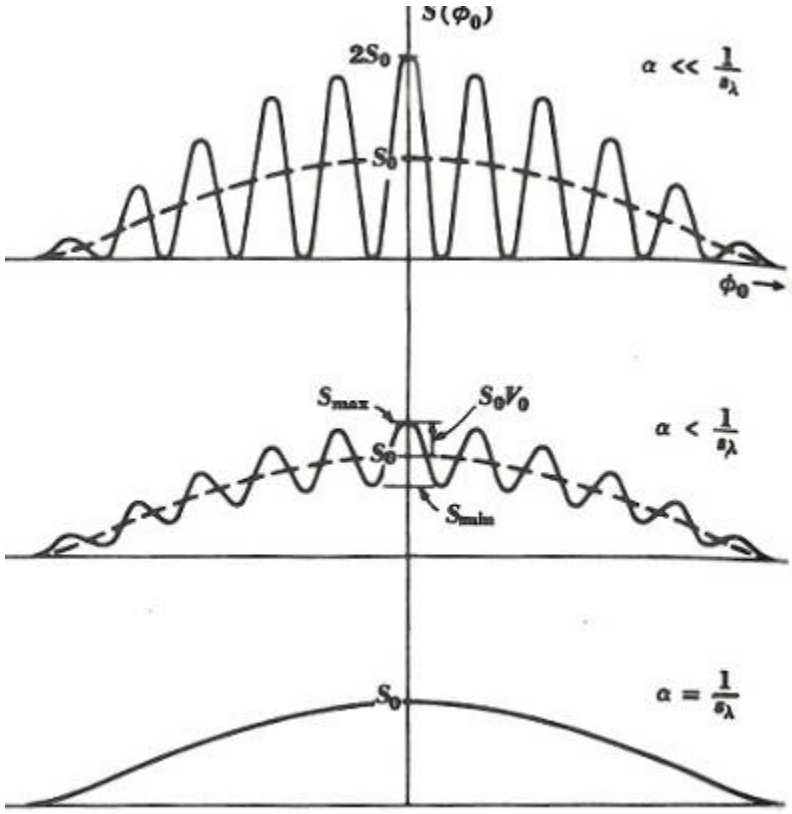

Figure B.4: Interferometer pattern (a) for point sources; (b) for a uniform extended source of angle $\alpha < 1/s_\lambda$; and (c) for a uniform extended source of angle $\alpha = 1/s_\lambda$.

Assuming that the observations are made at the meridian or that the source is tracked by the individual array elements, so that $|E_n(\phi)|^2 = 1$ becomes

$$S(\phi_0, s_\lambda) = S_0 + \int_{-\alpha/2}^{+\alpha/2} B(\phi) \cos\left[2\pi s_\lambda \sin(\phi_0 - \phi)\right] d\phi \qquad \text{(Y-8)}$$

If the source is small, so that $\phi_0 - \phi << \pi$, we may write

$$S(\phi_0, s_\lambda) = S_0 + \cos 2\pi s_\lambda \phi_0 \int_{-\alpha/2}^{+\alpha/2} B(\phi) \cos 2\pi s_\lambda \phi d\phi + \sin 2\pi s_\lambda \phi_0 \int_{-\alpha/2}^{+\alpha/2} B(\phi) \sin 2\pi s_\lambda \phi d\phi \qquad \text{(Y-9)}$$

Or $S(\phi_0, s_\lambda)$ may be expressed as the sum of a constant term and a variable term (sum of two terms). Thus,

$$S(\phi_0, s_\lambda) = S_0 \left[1 + V(\phi_{0,s_\lambda})\right] \qquad \text{(Y-10)}$$

where

$$V(\phi_0, s_\lambda) = \frac{1}{S_0}\cos 2\pi s_\lambda \phi_0 \int_{-\alpha/2}^{+\alpha/2} B(\phi)\cos 2\pi s_\lambda \phi d\phi + \frac{1}{S_0}\sin 2\pi s_\lambda \phi_0 \int_{-\alpha/2}^{+\alpha/2} B(\phi)\sin 2\pi s_\lambda \phi d\phi \qquad \text{(Y-11)}$$

The variable term may also be expressed as a cosine function with a displacement $\Delta\phi_0$. Thus,

$$V(\phi_0, s_\lambda) = V_0(s_\lambda)\cos[2\pi s_\lambda(\phi_0 - \Delta\phi_0)] \qquad \text{or} \qquad \text{(Y-12)}$$

$$V(\phi_0, s_\lambda) = V_0(s_\lambda)(\cos 2\pi s_\lambda \phi_0 \cos 2\pi s_\lambda \Delta\phi_0 + \sin 2\pi s_\lambda \phi_0 \sin 2\pi s_\lambda \Delta\phi_0 \qquad \text{(Y-13)}$$

The Quantity $V_0(s_\lambda)$ represents the amplitude of the observed lobe pattern, i.e., the *fringe amplitude*. It is also called the *fringe visibility* or simply the *visibility*. As a function of s_λ, it may be referred to as the *visibility function*. The angle $\Delta\phi_0$ represents the fringe displacement from the position with a point source. From (Y-11) and (Y-13) we have

$$V_0(s_\lambda)\cos 2\pi s_\lambda \Delta\phi_0 = \frac{1}{S_0}\int_{-\alpha/2}^{+\alpha/2} B(\phi)\cos 2\pi s_\lambda \phi d\phi \qquad \text{(Y-14)}$$

and

$$V_0(s_\lambda)\sin 2\pi s_\lambda \Delta\phi_0 = \frac{1}{S_0}\int_{-\alpha/2}^{+\alpha/2} B(\phi)\sin 2\pi s_\lambda \phi d\phi \qquad \text{(Y-15)}$$

It follows that

$$V_0(s_\lambda)e^{j2\pi s_\lambda \Delta\phi_0} = \frac{1}{S_0}\int_{-\alpha/2}^{+\alpha/2} B(\phi)e^{j2\pi s_\lambda \phi} d\phi \qquad \text{(Y-16)}$$

The quantity $V_0(s_\lambda)e^{j2\pi s_\lambda \Delta\phi_0}$ is called the *complex visibility function*. If the source is contained within a small angle, the limits can be extended to infinity without appreciable error, giving

$$V_0(s_\lambda)e^{j2\pi s_\lambda \Delta\phi_0} = \frac{1}{S_0}\int_{-\alpha/2}^{+\alpha/2} B(\phi)e^{j2\pi s_\lambda \phi} d\phi \qquad \text{(Y-17)}$$

According to (Y-17), the complex visibility function is equal to the Fourier transform of the source brightness distribution (times $1/S_0$). By the inverse Fourier transform we obtain

$$B(\phi_0) = S_0\int_{-\alpha/2}^{+\alpha/2} V_0(s_\lambda)e^{j2\pi s_\lambda \Delta\phi_0} e^{-j2\pi s_\lambda \phi_0} ds_\lambda \qquad \text{or} \qquad \text{(Y-18)}$$

$$B(\phi_0) = S_0\int_{-\alpha/2}^{+\alpha/2} V_0(s_\lambda)e^{-j2\pi s_\lambda(\phi_0 - \Delta\phi_0)} ds_\lambda \qquad \text{(Y-19)}$$

According to (Y-18) and (Y-19), the true brightness distribution of a source may be obtained, in principle, as the Fourier transform of the complex visibility function (an observed quantity).

To do this in practice requires observations at suitable internals out to sufficiently large spacings, a high source signal-to-noise ratio, and no other (confusing) sources of significant flux density in the individual element response pattern. Thus, there are practical limits to the detail with which the source distribution can be determined. According to Bracewell(1958), the spacing interval need be no smaller than 1/α, where α is the full source extent.

B.2 The Phase-switched (Multiplying) Interferometer

The interferometer of Fig. B.1 discussed earlier is of the simplest type, in which the voltages of the two antenna elements are continuously added. In the phase of one of the elements is periodically reversed and the output of the receiver reversed in synchronism, as suggested in Fig. B.5, a *phase-switched* interferometer results, which give the visibility without an additive constant in the output (Ryle, 1952). One method of reversing the phase of an array element is to insert ore remove one –half wavelength of transmission line.

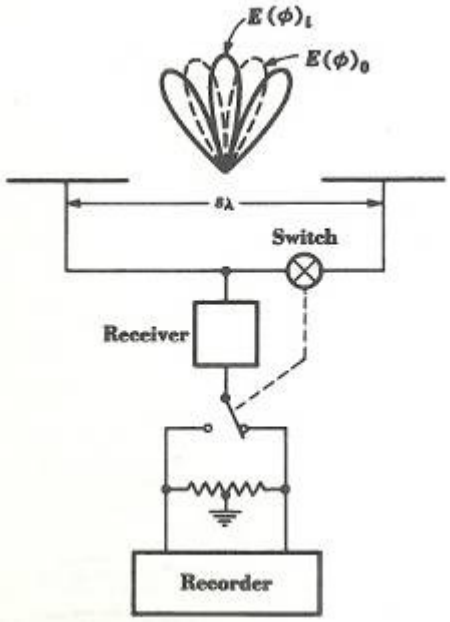

Figure B.5: Phase-switched interferometer with patterns shown for in-phase (solid) and out-of-phase (dashed) conditions.

When the antenna elements are in phase, the far-field patter is

$$E(\phi)_i = E_0(\phi)\left[e^{j(\psi/2)} + e^{-j(\psi/2)}\right] \qquad \text{(Y-20)}$$

where $E_0(\phi)$ = normalized field pattern of individual array element, $\psi = 2\pi s_\lambda \sin\phi$. In the pahse-reversed, or out-of-phase, condition the pattern is

$$E(\phi)_0 = E_0(\phi)\left[e^{j(\psi/2)} - e^{-j(\psi/2)}\right] \quad \text{(Y-21)}$$

The relative power pattern in the two cases are

$$P(\phi)_i = \left|E_0(\phi)\right|^2\left[e^{j(\psi/2)} + e^{-j(\psi/2)}\right]\left[e^{j(\psi/2)} + e^{-j(\psi/2)}\right]^* \quad \text{and} \quad \text{(Y-22)}$$

$$P(\phi)_0 = \left|E_0(\phi)\right|^2\left[e^{j(\psi/2)} - e^{-j(\psi/2)}\right]\left[e^{j(\psi/2)} - e^{-j(\psi/2)}\right]^* \quad \text{(Y-23)}$$

The system output is then proportion to the difference of the two patterns so that the recorded pattern is given by

$$P(\phi) = P(\phi)_i - P(\phi)_0 = 2\left|E_0(\phi)\right|^2\left(e^{j\psi} + e^{-j\psi}\right) \quad \text{(Y-24)}$$

or normalized by

$$P_n(\phi) = \left|E_n(\phi)\right|^2 \cos\psi = \left|E_n(\phi)\right|^2 \cos(2\pi s_\lambda \phi) \quad \text{(Y-25)}$$

For $|E_n(\phi)|_2 \approx 1$ the recorded flux density for a source of brightness distribution $B(\phi)$ and extent α is then

$$S(\phi_0, s_\lambda) = \int_{-\alpha/2}^{+\alpha/2} B(\phi)\cos\left[2\pi s_\lambda \sin(\phi_0 - \phi)\right]d\phi \quad \text{(Y-26)}$$

Thus, the phase-switched interferometer produces a fluctuating output of average value zero. In other words, there is no constant additive term ($=S_0$) as in (Y-8). The outputs of a simple (unswitched) and a phase-switched interferometer are compared in Fig. B.6

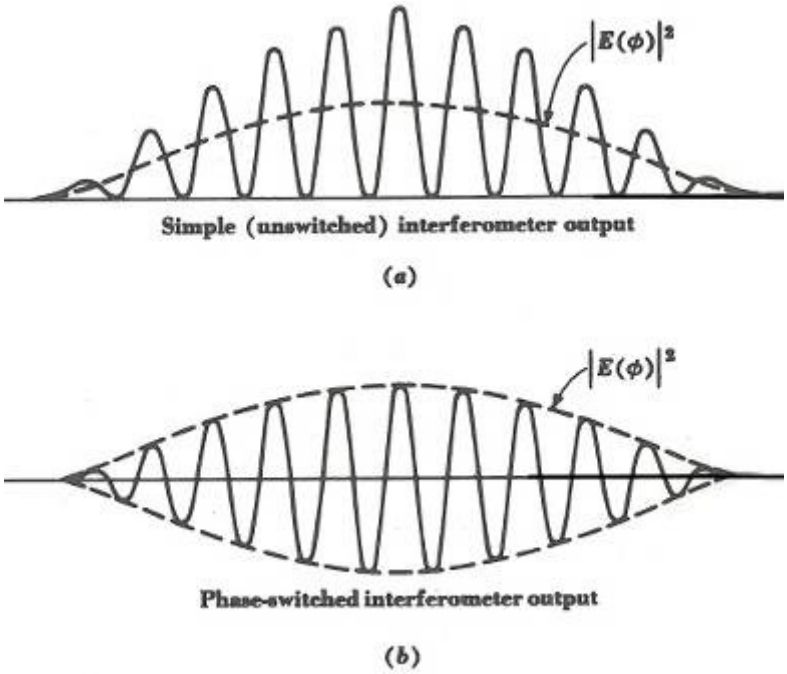

Figure B.6: (a) Output of simple, unswitched interferometer; (b) output of phase-switched interferometer.

The autocorrelation function of the aperture distribution ofor a phase-switched interferometer is indicated in Fig. B.7. This type of interferometer has the spatial-frequency characteristics of a bandpass filter. By contrast, the simple unswitched interferometer has the properties of a low-pass plus bandpass filter (Fig. B.2), while a continuous-specturm antenna is like a low-pass filter.

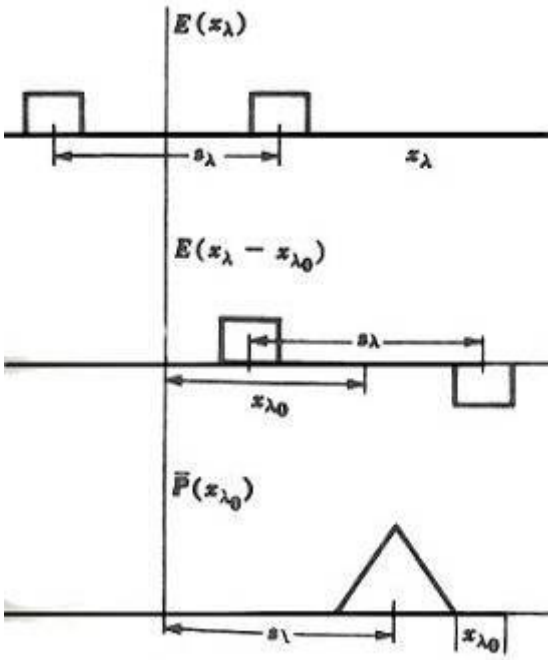

Figure B.7: The autocorrelation function of the aperture distribution of the phase-switched interferometer has the spatial frequency response $\overline{P}(x_{\lambda_0})$ of a bandpass filter.

The elements in the interferometers discussed thus far have been assumed to be identical. Let us now consider the more general case of two dissimilar elements, 1 and 2, as in Fig. B.8. For the case of phase switching, it can be readily shown that the relative power pattern is given by

$$P(\phi) = E_1(\phi)E_2^*(\phi)e^{j\psi} + E_1^*(\phi)E_2(\phi)e^{-j\psi} \qquad \text{(Y-27)}$$

where $E_1(\phi)$ = far-field pattern of element 1, $E_2(\phi)$ = far-field pattern of element 2, $\psi = 2\pi s_\lambda \sin\phi$. If the elements are identical [$E_1(\phi) = E_2(\phi)$], (Y-27) reduce to the same pattern as in (Y-25). If the elements are symmetrical, so that $E_1(\phi) = E_1^*(\phi)$ and $E_2(\phi) = E_2^*(\phi)$ (all lobes of phase 0 or π), the relative power pattern (Y-27) becomes

$$P(\phi) = E_1(\phi)E_2(\phi)\cos\psi \qquad \text{(Y-28)}$$

This is the general relation for a two-element phase-switched interferometer with symmetrical but dissimilar elements. The power pattern is seen to be proportional to the product of the field patterns of the individual elements. Hence, the phase-switched interferometer is sometimes referred to as a *multiplying* type. The voltage delivered by one element is proportional to the square root of its aperture area, so that the received power and the overall system aperture are proportional to the geometric mean of the two element aperture areas. Thus,

$$P \propto \sqrt{A_1 A_2} \tag{Y-29}$$

where P is received power, A_1 is aperture area of element 1, A_2 is aperture area of element 2.

If the spacing between the elements is reduced to zero, so that the elements form a cross (Mills and Little, 1953; Mills, 1963), we have, neglecting constrants, that (Y-27) reduced to

$$\begin{aligned} P(\phi) &= E_1(\phi)E_2^*(\phi) + E_1^*(\phi)E_2(\phi) \\ &= \mathrm{Re}\,E_1(\phi)\,\mathrm{Re}\,E_2(\phi) + \mathrm{Im}\,E_1(\phi)\,\mathrm{Im}\,E_2(\phi) \end{aligned} \tag{Y-30}$$

If the elements are symmetrical, the patterns are entirely real, so that (Y-30) reduces to

$$P(\phi) = E_1(\phi)E_2(\phi) \tag{Y-31}$$

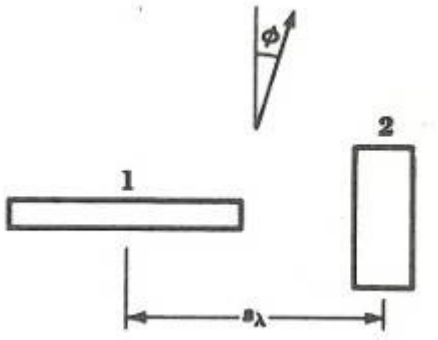

Figure B.8: Interferometer with two dissimilar elements.

B.3 The Multielement, or Grating, Interferometer

In [a previous section], an array of *n* sources of equal amplitude and spacing was discussed, and the far-field pattern was shown to be

$$E(\phi) = E_0(\phi)\frac{\sin(n\psi/2)}{\sin(\psi/2)} \tag{Y-32}$$

where $\psi = 2\pi d_\lambda \sin\phi$, and d_λ is spacing between elements, wavelengths, ϕ is angle from perpendicular to array, and n is number of sources. For a long array ($nd\lambda$ large) the beam width between first nulls (BWFN) of the main lobe (at $\phi = 0$) is given by

$$BWFN = \frac{2}{nd_\lambda}\,rad \tag{Y-33}$$

If d_λ exceeds unity, side lobes appear which are equal in amplitude to the main lobe. These so-called *grating lobes* havea spacing from the main lobe of

$$\phi_G = \sin^{-1}\frac{m}{d_\lambda} rad \qquad \text{where m = 1, 2, 3 . . . .} \qquad \text{(Y-34)}$$

If dλ >> 1, this reduces approximately to

$$\phi_G = \frac{m}{d_\lambda} rad \qquad \text{(Y-35)}$$

Now if ϕ_G is greater than the source extent, only one large lobe of the pattern will be on the source at a time, as suggested in Fig.B.9. To avoid confusion effects there must be on other sources of significant strength in the grating lobes. This multielement, or grating type of interferometer arrangement has been used by Christiansen and Warburton (1953) for the sun, effect of a succession of single-lobe scans being obtained as the sund drifts through the pattern. The sun is strong source, so that the grating lobes off the sun contribute relatively little to the received power.

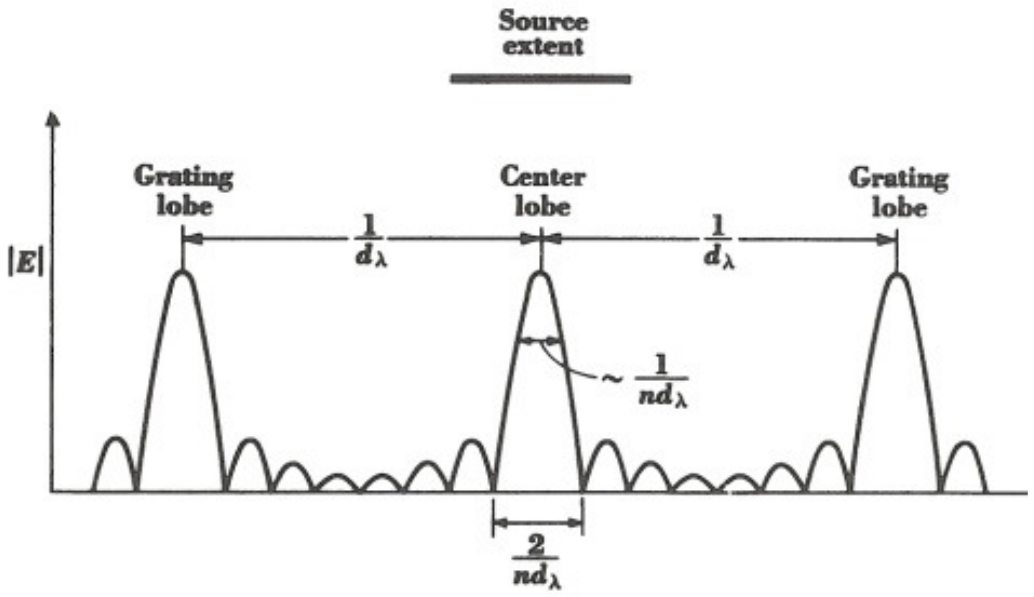

Figure B.9: Grating interferometer with grating-lobe spacing ϕ_G larger than source extent.

With a two-element interferometer of spacing s_λ equal to nd_λ, lobes or fringes would be obtained with a BWFN = $1/nd_\lambda$, or half the width in (Y-33). However, the next large lobe would be at the same angular distance (= $1/nd_\lambda$). The grating enterferometer has a BWFN = $2/nd_\lambda$ and a HPBW about half this, the same as a

continuous array of length nd_λ. The grating-lobe spacing is $1/d_\lambda$, or *n* times as large as the HPBW.

The source extent α, in the case of the sun is about ½°. Hence, for a grating interferometer *d* should be no more than 114 wavelengths. Taking $d = 100\lambda$ and $n = 32$ yields $BWFN = 2/nd_\lambda = 0.036°$ and $HPBW \approx 1/nd_\lambda = 0.018°$. Thus, in this case the beam width is sufficiently small compared to the source extent to reveal considerable detail.

It is assumed that the directivity of the individual elements is not enough to affect the pattern near $\phi = 0$. To suppress all grating lobes including the first would require an individual-element aperture of the order of d_λ. This would put the first null on the first grating lobe, but the array is now equivalent to a continuous aperture. The advantage of the grating interferometer, also sometimes called a *suppressed-lobe interferometer*, is the economy of a partially filled aperture to give the narrow beam width (high resolution) of a long continuous aperture for the case of strong sources of extent less than $1/d_\lambda$. However, the sensitivity is less than for the continuous aperture, the effective aperture of the system being equal only to the sum of the effective aperture of the individual elements.

References

[1] Kenneth P. Walsh, Brian Schulkin, Dale Gary, John F. Federici, Robert Barat, David Zimdars, "Terahertz near-field interferometric and synthetic aperture images", *Proceedings of SPIE Vol. 5411 2004*.

[2] Alexander M. Sinyukov, Aparajita Bandyopadhyay, Amartya Sengupta, Robert B. Barat, Dale E. Gray, Zoi-Heleni Michalopoulou, David Zimdars, and John F. Federici, "Terahetz interferometric image of a concealed object", *Proceedings of SPIE Vol. 6373* 2006.

[3] Alexander M. Sinyukov, Robert B. Barat, Dale E. Gray, Zoi-Heleni Machalopoulou, Ivan Zorych, David Zimdars and John F. Federici , "Terahetz interferometic imaging of RDX", *Proceedings of SPIE Vol. 6549* 2007.

[4] Dwight Woolard, Elliott Brown, Michael Pepper, Michael Kemp, "Terahertz Frequency Sensing and Imaging: A time of Reckoning Future Applications?" *IEEE* 2005.

[5] Kraus, John D., and Martti E. Tiuri. *Radio Astronomy*. Powell, OH: Cynus-Quasar, 1980.

[6] Alexander M. Sinyukov, Aparajita Bandyopodhyay, Amartya Sengupta, Robert B. Barat, Dale E. Gray, Zoi-Heleni Michalopoulou, David Zimdars and John F. Federici, "Terahetz interferometric and synthetic aperture images", *Proceedings of SPIE Vol. 6212* 2006.

[7] A. Goltsman, C. Dietlein, D.A. Wikner, O. Kilic, A.I. Zaghloul, "Three-Dimensional Terahertz Interferometric Imaging System for Concealed Object Detection", Presentation at URSI EMTS 2010, Berlin, Germany

[8] A. Goltsman and A.I. Zaghloul, "Interferometric Imaging at Terahertz Frequencies for Concealed Object Detection", Invited Paper, IEEE Microwave Theory and Techniques Workshop on Terahertz Device Characterization and Security Applications, Honolulu, Hawaii, June 2007.

[9] A. Goltsman and A.I. Zaghloul, "Three-Dimensional Interferometric Imaging at Terahertz Frequencies Using Three-Dimensional Spiral Array", 33rd International Conference on Infrared, Millimeter, and Terahertz Waves, Pasadena, California, September 2008.

[10] A. Goltsman and A.I. Zaghloul, "A Three-Dimensional Antenna Array for Terahertz Sensing", IEEE Conference on Sensors, Christchurch, New Zealand, October 2009.